Illuminating the mechanism and allosteric behavior of NanoLuc luciferase

Michal Nemergut[1,2,#], Daniel Pluskal[1,#], Jana Horackova[1,#], Tereza Sustrova[1,#], Jan Tulis[1], Tomas Barta[3], Racha Baatallah[4], Glwadys Gagnot[4,5], Veronika Novakova[1,2], Marika Majerova[1], Sérgio M. Marques[1,2], Martin Toul[1,2], Jiri Damborsky[1,2], David Bednar[1,2], Zbynek Prokop[1,2], Yves L. Janin[6], and Martin Marek[1,2,*]

1. Loschmidt Laboratories, Department of Experimental Biology and RECETOX, Faculty of Science, Masaryk University, Kamenice 5, Bld. C13, 625 00 Brno, Czech Republic
2. International Clinical Research Center, St. Anne's University Hospital Brno, Pekarska 53, 656 91 Brno, Czech Republic
3. Department of Histology and Embryology, Faculty of Medicine, Masaryk University, Kamenice 753/5, 625 00 Brno, Czech Republic
4. Unité de Chimie et Biocatalyse, Institut Pasteur, UMR 3523, CNRS, 28 rue du Dr. Roux, 75724 Paris Cedex 15, France
5. Université de Paris, 12 rue de l'école de Médecine, 75006 Paris, France.
6. Structure et Instabilité des Génomes (StrInG), Muséum National d'Histoire Naturelle, INSERM, CNRS, Alliance Sorbonne Université, 75005 Paris, France

[#] These authors contributed equally to this study.

* Corresponding author: martin.marek@recetox.muni.cz

Abstract

NanoLuc, a superior β-barrel fold luciferase, was engineered 10 years ago but the nature of its catalysis remains puzzling. Here experimental and computational techniques were combined, revealing that imidazopyrazinone luciferins bind to an intra-barrel catalytic site but also to an allosteric site shaped on the enzyme surface. Binding to the allosteric site prevents simultaneous binding to the catalytic site, and vice versa, through concerted conformational changes. We demonstrate that restructuration of the allosteric site can dramatically boost the luminescent reaction in the remote active site. Mechanistically, an intra-barrel arginine coordinates the imidazopyrazinone component of luciferin to attack O_2 via a radical charge-transfer mechanism, as well as it protonates the excited amide product to secure high emission intensity. Concomitantly, an aspartate, supported by two tyrosines, fine-tune the electronic state of amide product, promoting the formation of the blue color emitter. This information is critical to engineering the next-generation of light-producing biosystems.

Keywords: bioluminescence; light emission; luciferase; furimazine; coelenterazine; NanoLuc; catalysis

Introduction

Bioluminescence is a fascinating phenomenon involving the emission of light by a living organism.[1] Hence, there is huge interest in harnessing bioluminescent systems not only to design ultrasensitive optical bioassays but also to enable sustainable and environmentally friendly lighting technologies.[2–5] Bioluminescent systems generate "cold light" via the oxidation of a substrate (a luciferin), which is catalyzed by a group of enzymes called luciferases.[1]

In 1978, Shimomura and co-workers probed bioluminescence of *Oplophorus gracilirostris*, a deep shrimp that ejects a cloud of brightly luminescent secretion from the base of antennae as a defense mechanism against predation.[6] The identified *O. gracilirostris* luciferase, henceforth referred to as OLuc, has quaternary structure composed of two ~35 kDa and two ~19 kDa subunits.[7] Like many marine luciferases, it oxidizes coelenterazine (CTZ), an imidazopyrazinone containing luciferin, into a coelenteramide (CEI), in a cofactor-independent decarboxylating reaction to generate blue light (λ_{max} = ~460 nm).[6] Cloning experiments showed that bioluminescent activity entirely relies on the smaller subunit.[7] Unfortunately, this smaller subunit, when recombinantly produced alone, does not retain many of the desirable properties evident in the native enzyme, as it is unstable and poorly soluble.[7] Therefore, structural optimization of the catalytic subunit by protein engineering was performed, hand in hand with the addition of a novel substrate called furimazine (FMZ), to create an innovative luciferase-luciferin pair, named NanoLuc (or NLuc) system.[8]

While the engineered NanoLuc still catalyzes native CTZ-to-CEI reaction, it displays superior specific activity for FMZ to furimamide (FMA) oxidation, up to 150-fold higher than firefly luciferase (FLuc) and *Renilla* luciferase (RLuc) toward their native substrates.[8] NanoLuc is a multipurpose technology that revolutionizes bioimaging, including the investigation of protein–protein and protein–ligand interactions, exploring gene regulation and cell signaling, monitoring protein stability, and development of bioluminescence resonance energy transfer (BRET)-based sensors.[4,9–15] However, despite its incredible technological and commercial success[8,10,11], the nature of its luciferin-binding site and mechanism by which it generates blue photons remain unknown. In addition, major drawbacks of the NanoLuc system are that the FMZ-luciferin is poorly soluble, possesses cytotoxic properties[16] and is substantially more expensive than widely accessible CTZ-luciferin.

In 2016, Tomabechi and co-workers determined the crystal structure of apo-NanoLuc.[17] The structure consists of eleven antiparallel β-strands (S1-11) forming a β-barrel that is capped by 4 α-helices (H1-4), displaying structural similarity with distantly related fatty acid-binding proteins (FABPs).[17] The engineered NanoLuc, unlike the native OLuc, is reported as a monomeric enzyme, and it is anticipated that a luciferin binds to a central cavity of the β-barrel structure, where catalysis should occur.[17–19] In the

meantime, additional three crystal structures were determined and deposited in the PDB database[20] (PDB ID codes: 7MJB, 5IBO and 7VSX[19]), two complexed with decanoic acid and one with 2-(N-morpholino)ethanesulfonic acid (MES). Apparently, a key barrier to the deciphering of puzzling mechanism of NanoLuc catalysis is the unavailability of structural data on catalytically favored luciferin-bound enzyme complexes.

Here we determined co-crystal structures of NanoLuc luciferase complexed with oxidized imidazopyrazinone luciferins as well as a non-oxidizable substrate analogue azacoelenterazine[21]. We demonstrate that luciferins bind not only to an intra-barrel catalytic site but also to a secondary, allosteric site, shaped on the molecular surface of enzyme. Binding to the allosteric site prevents simultaneous binding to the catalytic site through the so-called homotropic negative allostery mechanism. Moreover, we reveal molecular details of NanoLuc catalytic machinery and delineate its reaction mechanism. This information is critical to engineering of next-generation luciferase luciferin pairs for ultrasensitive optical bioassays and renewable light-producing technologies.

Results

Identification of a luciferin-binding site on enzyme surface

To obtain atomistic insights into the action mechanism of NanoLuc, we found new crystallization conditions for the obtaining of diffraction-quality crystals, which were then extensively soaked in the luciferin-supplemented mother liquor. Diffraction experiments yielded high-resolution data, and structures were solved by molecular replacement (**Supplementary Table 1**). Notably, the NanoLuc is packed in the crystals as a back-to-back dimer of two homodimers (crystallographic homotetramer) with a central pore, where all four carboxy-terminal ends are involved in the self-association. We identified a chloride ion that occupies the central pore, and it thus contributes to the homotetrameric association (**Supplementary Fig. 1**). Strikingly, apart from all intramolecular cavities, the crystal packing reveals several spacious pockets shaped on the molecular surface of NanoLuc luciferase, which might potentially serve as a luciferin-binding site (**Supplementary Fig. 1**).

Indeed, inspection of the electron density maps unambiguously revealed FMA, an amide product of FMZ oxidation, bound in a voluminous pocket found on the molecular surface of the enzyme, and localized at the crystallographic homodimer interface (**Fig. 1a**). Strikingly, while previously determined decanoic acid-bound NanoLuc crystal structures are composed of the four symmetry-related monomers that form a perfect symmetric homodimers (PDB ID codes 7MJB and 5IBO), our luciferin-soaked

structures revealed a symmetry breaking in the dimer interface. The origin of this interface asymmetry lies in the rearrangement of a structural element encompassing a helix H4, a loop L7, and a strand S4 (**Fig. 1b-c**). Due to this conformational change, the FMA-bound pocket is less spacious (closed) than a corresponding pocket located on the opposite side of the two-fold rotational axis. The B-factor analysis demonstrated that both the helix H4 and adjacent loop L7, unlike the β-barrel core, are highly mobile elements, allowing pocket gating (**Fig. 1d**). PISA calculations[22] showed that the crystallographic dimer interface area is ~830 $Å^2$, which represents ~9.2% of the total solvent-accessible surface area of the monomer (~8 995 $Å^2$). There are 27 (chain A) and 28 (chain B) interfacing residues involved in the dimer interface, which is a significant portion of 169-residue protein (**Fig. 1e-f**).

Nature of the surface-localized luciferin-binding site

The luciferin-binding pocket is defined by the groove on the β-barrel surface of one monomer (chain A), shaped by long strands S3 and S5, building the pocket bottom (**Fig. 1g-h**). The sides of the pocket are formed by strands S1 and S4 of the same monomer. The lid of the pocket is secured by an amino-terminal part, predominantly residues E4, V7, G8 and D9, of a second monomer (chain B). The back-side of the pocket is closed by the carboxy-terminal tails (residues 166–169) of both chains (**Fig. 1h**).

FMA-luciferin adopts a crab-like conformation, where the R^1 2-(furan-2-yl) and R^3 8-benzyl substituents constitute the claw-like structures, while the R^2 6-phenyl substituent is the tail (**Fig. 1g**). The latter part, 6-phenyl moiety, is deeply buried in the pocket, where it is anchored through multiple non-polar and hydrophobic contacts with D9, I41 and I167 (**Fig. 1h**). The 8-benzyl substituent makes hydrophobic contacts with V7 (chain B) and V83 (chain A). The 2-(furan-2-yl) is positioned in proximity to a tyrosine-tyrosine dyad, allowing T-shaped π-stacking with Y81 (4.5 Å), and hydrophobic contacts with Y94 (4.3 Å). Moreover, the 2-(furan-2-yl) makes a π-cation interaction with the side chain of K89.

The acetamidopyrazine core is shielded by the side chain of R43, which at the same time makes both a bidentate hydrogen bonding with the carboxylate of D9 and a hydrogen bonding with the main-chain carbonyl of G8, provided by the second monomer (chain B). Crucially, the FMA carbonyl oxygen makes a hydrogen bond with the carboxylate of D55 (2.4 Å), while the amide nitrogen is hydrogen bonded with the side chain of K89 (2.4 Å) (**Fig. 1h**). As shown in **Fig. 1i**, several pocket-shaping residues (e.g. E4, R43 and R166), played a key role during the development of NanoLuc.[8]

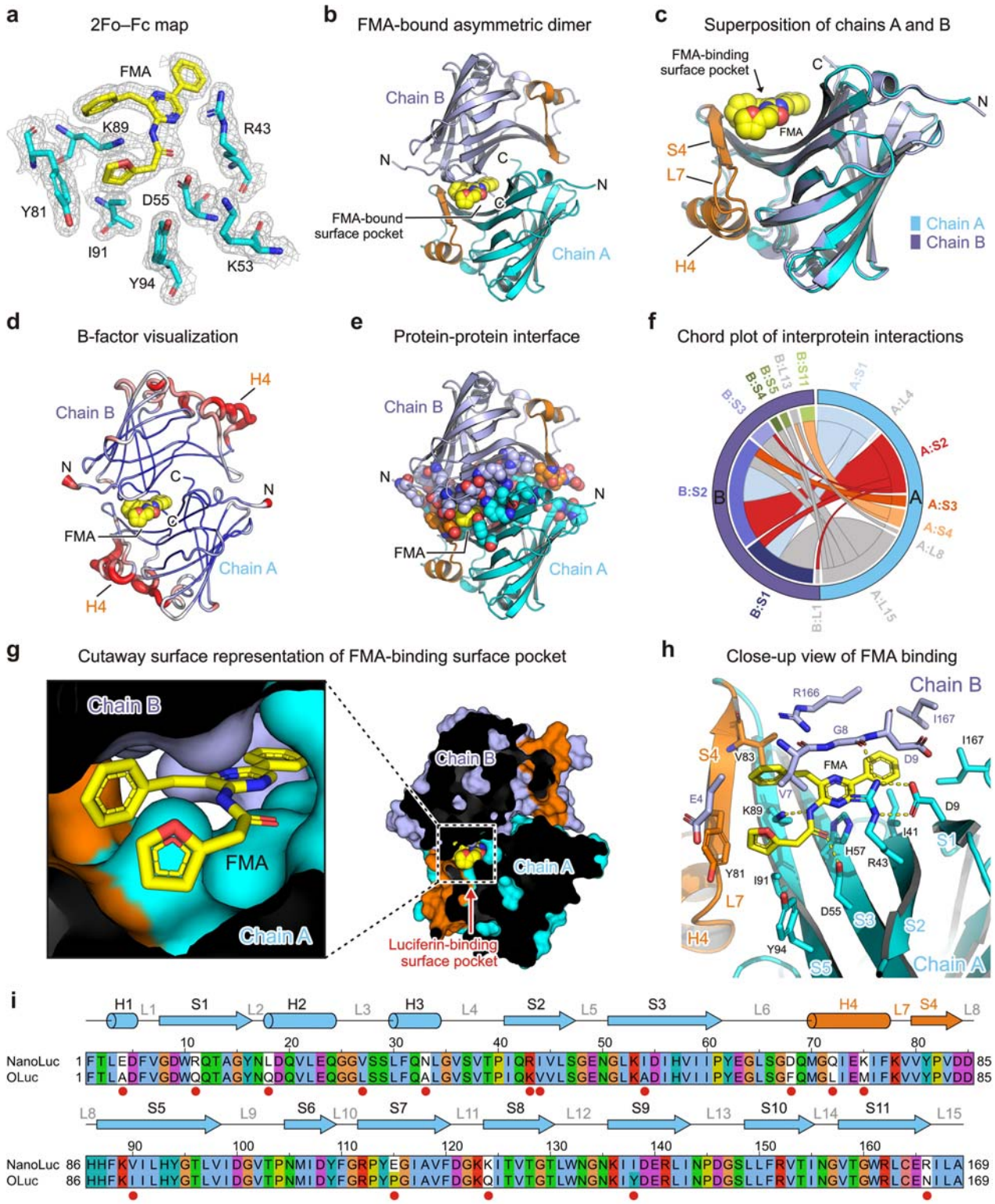

Fig. 1. The structure of FMA-bound crystallographic homodimer of NanoLuc luciferase. (a) 2Fo-Fc electron density (contour level 1.2 σ) at the FMA-luciferin binding site. (b) Cartoon representation of the overall structure of NanoLuc asymmetric dimer (chain A in cyan and chain B in blue) with bound FMA luciferin (yellow). (c) Superposition of chain A (cyan) and chain B (blue). The structural element responsible for symmetry breaking,

encompassing helix H4, loop L7 and strand S4, is colored orange. (d) B-factor putty representation of NanoLuc homodimer. (e) Dimer interface visualization. All residues involved in the dimer interface are shown as space-filling spheres. FMA is shown as yellow spheres. (f) Chord plot of interactions between chains A and B in NanoLuc dimer, calculated and visualized by Protein Contact Atlas[23]. (g) Cutaway surface representation of FMA-bound NanoLuc dimer. (h) Close-up view of FMA-binding pocket with residues creating the active site in stick representation. Key hydrogen bonds are shown as dashed yellow lines. (i) Sequence alignment between NanoLuc and the catalytic unit of *O. gracilirostris* luciferase (OLuc). Secondary structure elements found in NanoLuc are shown above the alignment. Amino acid residues mutated during the NanoLuc engineering[8] are labeled with the red dot. The numbering indicated above the alignment corresponds to NanoLuc structure (PDB ID: 5B0U)[17].

One pocket, two radically different luciferin-binding modes

While the FMA adopts crab-like conformation, employing the tail part to be deeply inserted in the luciferin-binding pocket (**Fig. 1g**), a radically different binding mode is observed for the CEI-luciferin (**Fig. 2a-c**). Compared to the FMA-luciferin, the CEI is horizontally rotated by ~120°, allowing its 2-(*p*-hydroxyphenyl)acetamide moiety to be deeply buried in the pocket. Though the FMA-luciferin makes interactions only within the asymmetric dimer (chains A and B), the hydroxyl group of CEI R^1 2-(*p*-hydroxyphenyl) makes a hydrogen bond (3.4 Å) with the carboxylate of E165 in neighboring chain C (**Fig. 2d**). Additionally, the CEI carbonyl group forms a hydrogen bond with the carboxylate of D9 (3.1 Å), and the nitrogen atoms of the central pyrazine ring are hydrogen bonded with the side chains of K89 (2.9 Å) and R166 (2.5 Å). The R^2 6-(*p*-hydroxyphenyl) moiety makes contacts with Y81 and D5 (**Fig. 2d**). The superposition of FMA and CEI binding modes demonstrates that both luciferins bind to the same pocket, but in a dissimilar fashion (**Fig. 2e**), highlighting luciferin-specific molecular recognition determinants. Moreover, the luciferin-binding site perfectly overlaps with the fatty acid-binding site, where decanoic acid molecules are found in the two previously determined NanoLuc complex structures, highlighting this site as a versatile ligand-binding pocket (**Supplementary Fig. 2**). Moreover, we found in our co-crystal structures that polyethylene glycol (PEG) molecules, originating from the mother liquor, bind in this pocket too (**Supplementary Fig. 3**).

From the superposition of our co-crystal structures, it is evident why neither CTZ nor its oxidized derivative CEI can bind to the luciferin-binding surface pocket in the same way as the one employed by FMZ or its oxidized catalytic product FMA. As shown in **Supplementary Fig. 4**, the CEI molecule is bulkier than the FMA, producing structural clashes when modeled in the FMA-preferred binding mode. Specifically, the 2-(*p*-hydroxyphenyl)acetamide moiety would clash with the side chain of Y81, while the terminal 6-(*p*-hydroxyphenyl) group would be in a clash with I167 residue in the pocket bottom. By contrast, the size and shape of FMZ luciferin predestine its 2-(furan-2-ylmethyl) substituent to be locked

by a tyrosine-tyrosine gate formed by the side chains of Y81 and Y94 residues, while the 8-benzyl substituent is complementary with the hydrophobic environment of the pocket bottom (**Supplementary Fig. 4**).

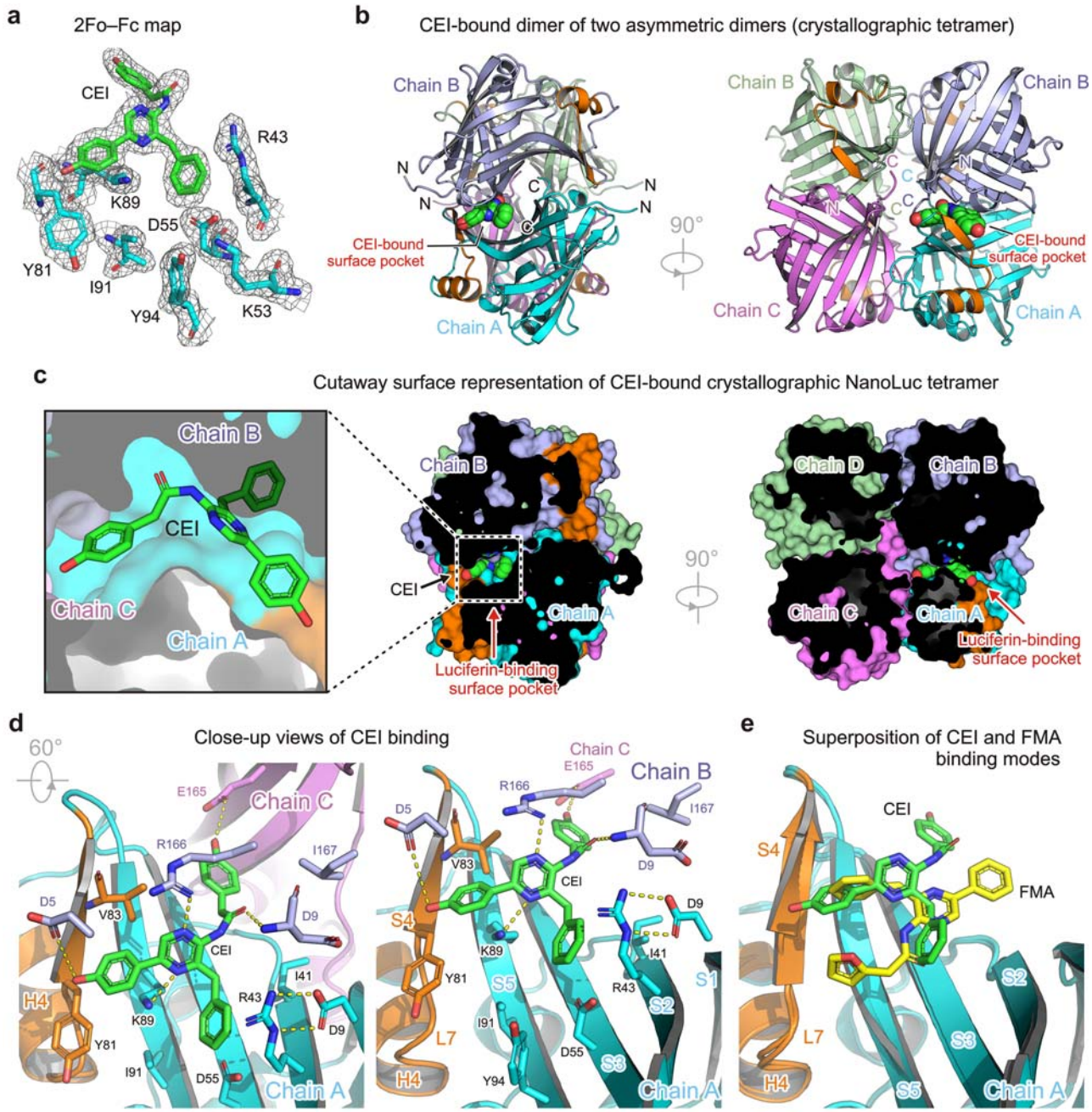

Fig. 2. The structure of CEI-bound crystallographic homotetramer of NanoLuc luciferase. (a) 2Fo-Fc electron density (contour level 1.2 σ) at the CEI-luciferin binding site. (b) The overall structure of NanoLuc homotetramer, composed of two tail-to-tail asymmetric homodimers (chain A in cyan, chain B in blue, chain C in violet and chain D in green). The CEI luciferin is shown as space-filling spheres (green). (c) Cutaway surface representation of CEI-

bound NanoLuc tetramer. (d) Close-up views of CEI-binding pocket with residues creating the active site in stick representation. Key hydrogen bonds are shown as dashed yellow lines. (e) Superposition of FMA (yellow) and CEI (green) binding modes.

Catalytic effects of mutations in the luciferin-binding surface site

Interestingly, seven out of sixteen amino acid residues mutated during the engineering of NanoLuc luciferase[8] (**Fig. 1i**), are spread around the luciferin-binding surface pocket, meaning that in total 14 (2 × 7) mutated residues are localized at the crystallographic homodimer interface (**Supplementary Fig. 5**).

To probe the functional importance of amino acid residues forming the luciferin-binding surface pocket, we performed structure-guided mutagenesis, and studied the effect of these mutations on NanoLuc bioluminescence. All constructed mutants were expressed and purified as soluble proteins. As shown in **Fig. 3a**, we observed strikingly different behavior of many mutants when either FMZ or CTZ was used in the reaction, confirming the assumption that these two luciferins can be differently recognized by the enzyme. For instance, single-point mutations R43A, D55A and K89E exhibited a stronger reduction of FMZ-luminescence than that of CTZ-luminescence, which is in agreement with structural observations (**Figs. 1** and **2**). On the contrary, truncation of three C-terminal residues (del 167-169) or two-alanine extension of the C-terminal end (ext A170-A171) substantially decreased CTZ-luminescence but had a moderate effect on FMZ-luminescence, demonstrating that CTZ reaction relies on intact C-terminal end (**Fig. 3a**).

Strikingly, the most severe effect on both FMZ and CTZ luminescence was observed when a tyrosine-to-alanine mutation was introduced at position 94. The Y94A mutant severely compromised NanoLuc action through ~67- and ~130-fold reduction of catalytic efficiency (k_{cat}/K_m) with CTZ and FMZ, respectively (**Fig. 3b** and **Table 1**). Numerical kinetic analyses are provided in **Supplementary Figs. 6-11**. As seen in our co-crystal structures, the side chain of Y94, together with the side chain of Y81, constitute a tyrosine-tyrosine dyad gating the luciferin-binding surface pocket (**Fig. 3c**). The luminescence-emission spectra of the NanoLuc-Y94A mutant are red-shifted by ∼2 nm with FMZ, while the emission maximum with CTZ is blue-shifted by ∼1 nm (**Supplementary Fig. 12**). Moreover, we obtained diffraction-quality crystals of the NanoLuc-Y94A mutant and its structure was solved (**Fig. 3c**; **Supplementary Table 1**). Although this mutant was crystallized in identical conditions as the wild-type enzyme, it crystallized as perfectly symmetric dimer with no bound luciferin molecule. Collectively, our mutagenesis experiments suggested a mechanism of communication between the surface binding site and the intra-barrel catalytic site, which is compromised by the tyrosine-to-alanine mutation at the position 94.

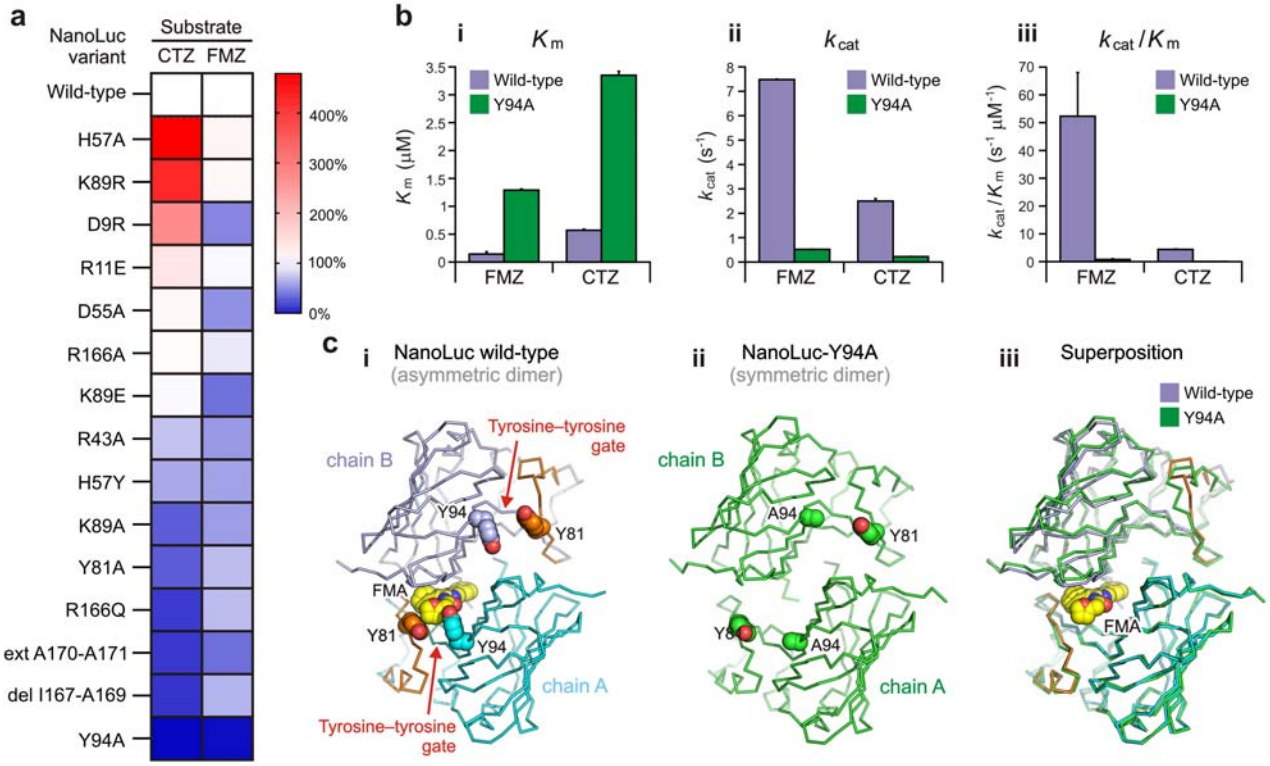

Fig. 3. Characterization of NanoLuc mutants. (a) Heat-map showing the relative luciferase activities of NanoLuc mutants with CTZ (left column) and FMZ (right column) luciferins. NanoLuc wild-type = 100%. (b) Comparisons of kinetic parameters (K_m, k_{cat} and k_{cat}/K_m) of NanoLuc wild-type (blue) and NanoLuc-Y94A mutant (green). (c) Structures of FMA-bound asymmetric dimer of NanoLuc wild-type (i) and luciferin-free symmetric dimer of NanoLuc-Y94A mutant (ii), and their superposition (iii). The tyrosine-tyrosine gate Y81 and Y94 (A94) residues and FMA-luciferin are shown as space-filling spheres.

Table 1. Kinetic parameters of NanoLuc luciferase mutants. Data are presented as mean with standard deviations (n=3).

Enzyme variant	K_m / μM	k_{cat} / s^{-1}	K_p / μM	k_{cat}/K_m / s^{-1} μM^{-1}
	CTZ-luminescence			
NanoLuc	0.57 ± 0.02	2.48 ± 0.05	0.256 ± 0.005	4.4 ± 0.2
NanoLuc-Y94A	3.74 ± 0.09	0.225 ± 0.004	0.79 ± 0.04	0.060 ± 0.001
NanoLuc-D9R/K89R	0.46 ± 0.01	16.8 ± 0.6	0.163 ± 0.006	37 ± 1
NanoLuc-D9R/H57A/K89R	0.77 ± 0.07	40 ± 4	0.23 ± 0.02	70 ± 7
	FMZ-luminescence			
NanoLuc	0.123 ± 0.004	7.88 ± 0.03	0.56 ± 0.01	64 ± 2
NanoLuc-Y94A	1.29 ± 0.02	0.519 ± 0.007	0.85 ± 0.02	0.402 ± 0.006
NanoLuc-D9R/K89R	0.157 ± 0.009	5.2 ± 0.1	0.39 ± 0.03	33 ± 2
NanoLuc-D9R/H57A/K89R	0.098 ± 0.005	2.74 ± 0.03	0.34 ± 0.02	28 ± 1

A conformational switch between open and closed β-barrel

Next, a comparison of ligand-free (apo-form) and ligand-bound NanoLuc structures revealed a conformational switch between the so-called open and closed states of the β-barrel structure (**Fig. 4a,b**). This conformational transition comprises several concerted structural re-arrangements, including unusual flipping of the β-strand S5. The open conformation of the β-barrel structure is captured in NanoLuc structures determined by Tomabechi[17] and Inouye[19]. One of the major hallmarks of this open conformation is that the side chain of H93 is exposed on the surface and concomitantly the side chain of Y94 is dipped inside the β-barrel structure, making the central cavity more voluminous, presumably to accommodate bulky luciferin molecule in the Michaelis enzyme-substrate complex. On the contrary, the complex structures with bound fatty acid or luciferin molecules in the surface binding site show the closed conformation, with the side chain of Y94 placed on the surface while the side chain of H93 is inserted in the β-barrel structure. The most striking feature is that the competences to bind luciferin either in the surface pocket or in the central putative catalytic site are mutually exclusive, implying the so-called homotropic negative allostery mechanism. This means that a luciferin molecule can be bound at one time either in the surface allosteric site (closed β-barrel structure) or in the intra-barrel catalytic site (open β-barrel structure), but never in both simultaneously (**Fig. 4)**.

We anticipate that the conformational switch between open and closed states of the β-barrel structure can be important for allosteric regulation of NanoLuc luciferase, and that the Y94 plays an integral role in this process. Moreover, when the β-barrel adopts its closed state, two chloride ions can bind in pre-formed intra-barrel chloride-binding sites, inactivating the catalytic machinery (**Fig. 4c-e**). Our structures thus provide structural basis for the reversible inhibition of NanoLuc luciferase by high concentration of chloride ions, as previously evidenced by Altamash and co-workers[18].

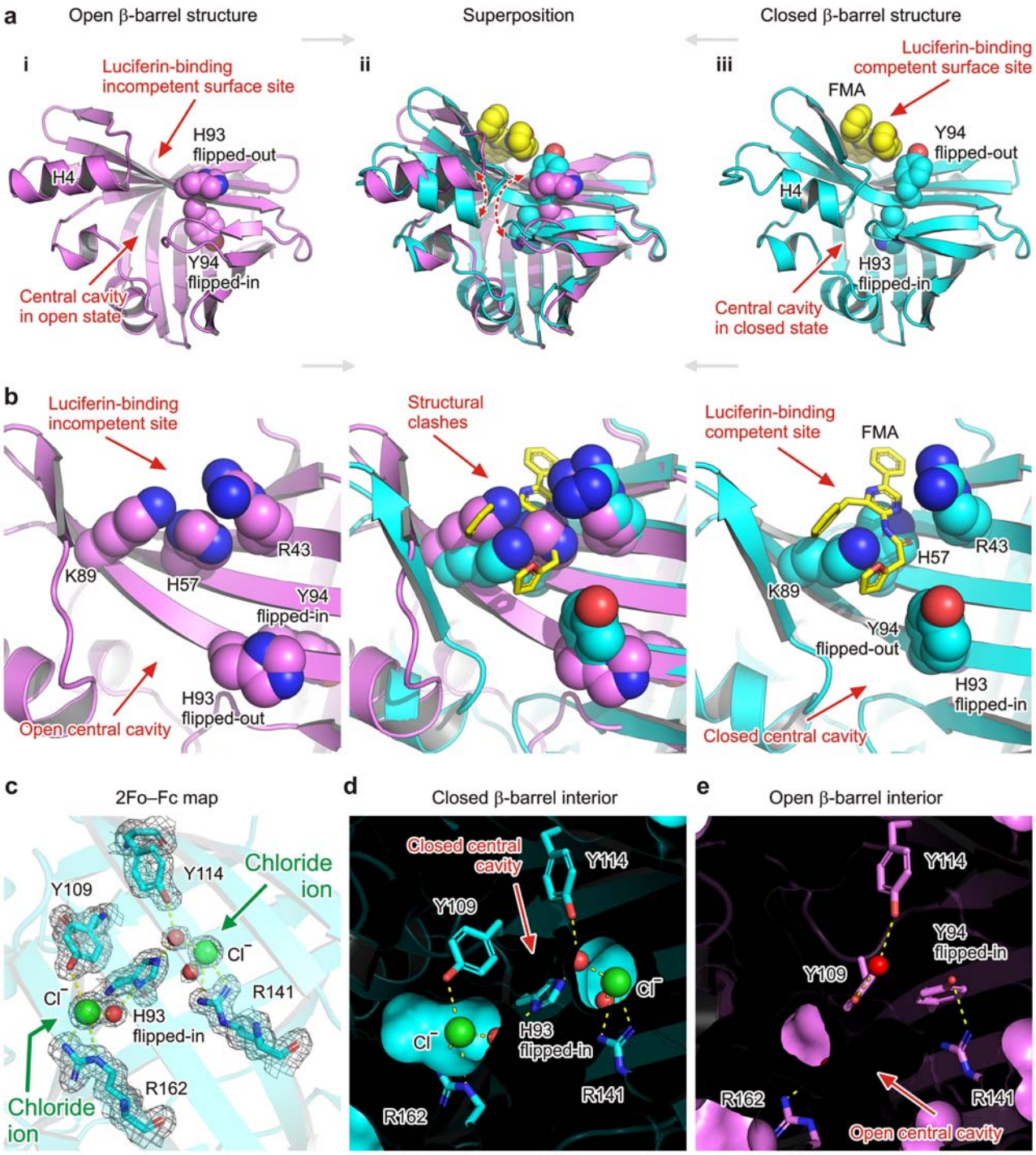

Fig. 4. Conformational switch between open and closed NanoLuc β-barrel structures. (a) Cartoon representations of (i) ligand-free apo-NanoLuc structure (PDB ID: 5B0U), (ii) FMA-bound NanoLuc structure, and (ii) their superposition. The H93 and Y94 residues and FMA-luciferin are shown as space-filling spheres. (b) Close-up views of (i) luciferin-binding surface pocket in ligand-free apo-NanoLuc structure (PDB ID: 5B0U), (iii) FMA-bound NanoLuc structure, and (ii) their superposition. R43, H57, K89, H93 and Y94 residues are shown as space-filling spheres, and the FMA luciferin is shown as yellow sticks. (c) 2Fo-Fc electron density (contour level 1.2 σ) at

the CBS-1 and CBS-2 sites. (D,E) Cutaway surface representations of NanoLuc β-barrel interior in a closed (d) and open (e) state. Note that in the closed β-barrel state, the two chloride ions are bound inside the β-barrel state.

Restructuring the allosteric site boosts CTZ-bioluminescence

As shown in **Fig. 3a**, not all single-point mutations caused functional impairment. Specifically, several mutations restructuring the allosteric site substantially and selectively increased bioluminescence with CTZ but not with FMZ. The most striking mutations, particularly D9R, H57A and K89R (**Fig. 5a**), individually induced up to ~4.5-fold enhancement of CTZ-bioluminescence. Subsequent combining of these mutations in corresponding double- and triple-mutants resulted in up to a □10-fold increase in CTZ-bioluminescence, while FMZ-bioluminescence was slightly decreased (**Fig. 5b**).

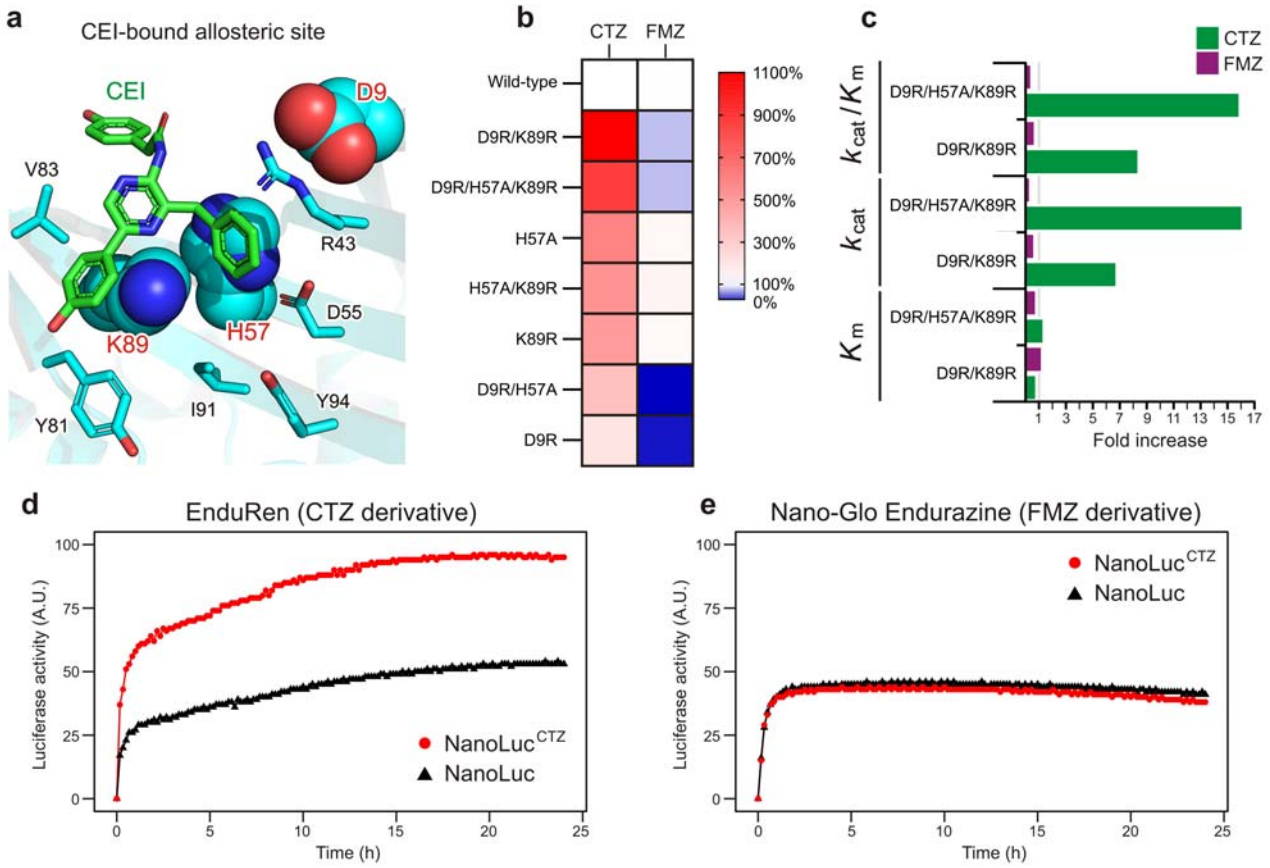

Fig. 5. Enhancement of NanoLuc catalysis toward CTZ through combinatorial mutagenesis of the allosteric site. (a) Close-up view of the CEI-bound luciferin-binding surface site of NanoLuc luciferase. Three residues, namely D9, H57 and K89, whose mutations increase bioluminescence with CTZ are shown as cyan space-filling spheres. The other protein residues are shown as cyan sticks, and the CEI-luciferin is shown as green sticks. (b) Heat-map showing the relative luciferase activities of NanoLuc mutants with CTZ (left column) and FMZ (right column) luciferins; NanoLuc wild-type = 100%. (c) Relative fold increases of kinetic parameters (K_m, k_{cat} and k_{cat}/K_m)

observed in the double NanoLuc-D9R/K89R and triple NanoLuc-D9R/H57A/K89R mutants; NanoLuc wild-type = 1. Absolute values of kinetic parameters (K_m, k_{cat} and k_{cat}/K_m) are summarized in **Table 1**. (d,e) Long-term live-cell bioluminescence imaging of cultured HEK293T cells expressing either original NanoLuc or engineered NanoLuc^{CTZ} and powered by EnduRen (d) or Nano-Glo Endurazine (e) substrate. The luciferase activities upon addition of corresponding luciferin were measured by LuminoCell device.[24]

The two top-ranking mutants, namely the double-mutant D9R/K89R and the triple mutant D9R/H57A/K89R, the latter mutant termed as NanoLuc^{CTZ}, were selected for comprehensive kinetic characterization to better understand why these mutations improved selectively bioluminescence with CTZ but not with FMZ. The luminescence-emission spectra of engineered NanoLuc^{CTZ} variants are red shifted by ~2 nm with CTZ-luciferin, while not affected with FMZ-luciferin (**Supplementary Fig. 12**). The kinetic analyses showed a 15.9-fold increase of catalytic efficiency (k_{cat}/K_m) with CTZ-luciferin, which was achieved through a 16.1-fold increase in k_{cat}, while the K_m and K_p values were not significantly affected. Importantly, the triple mutant, NanoLuc^{CTZ}, displayed catalytic efficiency with CTZ (k_{cat}/K_m = 70 ± 7 $s^{-1}.\mu M^{-1}$) which is very similar to that of the original NanoLuc with FMZ (k_{cat}/K_m = 64 ± 2 $s^{-1}.\mu M^{-1}$) (**Table 1**).

An engineered NanoLuc^{CTZ} is a superior in vivo reporter

We further engineered mammalian HEK293T cells to express either NanoLuc^{CTZ} or NanoLuc luciferase for long-term live-cell imaging experiments. Notably, we demonstrated that the NanoLuc^{CTZ} luciferase exhibits superior bioluminescence over the original NanoLuc in cell-based assays with EnduRen substrate (CTZ derivative), confirming its advantageous reporting properties (**Fig. 5d**). On the other hand, when the Nano-Glo Endurazine substrate (FMZ derivative) was used, the NanoLuc^{CTZ} and NanoLuc showed similar luciferase activities (**Fig. 5e**), which however only reached ~50% of NanoLuc^{CTZ} activity with EnduRen substrate (**Fig. 5d**). Collectively, our cellular experiments showed that the engineered NanoLuc^{CTZ} and EnduRen substrate represent a superior luciferase-luciferin reporting pair for long-term live-cell imaging applications, substantially surpassing the original NanoLuc/Nano-Glo Endurazine pair.

Capturing azacoelenterazine bound in the catalytic site

To obtain structural insights into the NanoLuc^{CTZ} catalysis, we attempted its co-crystallization with native CTZ or a non-oxidizable substrate analogue azacoelenterazine (azaCTZ) that we recently developed.[21] While no diffraction-quality crystals were obtained with CTZ, the co-crystallization with azaCTZ resulted in well-diffracting crystals, and corresponding complex structure was determined (**Supplementary Table 1**). Inspection of the electron density map unambiguously revealed azaCTZ molecule bound in the

catalytic cavity located inside its open state β-barrel structure (**Fig. 6a-c**). The azaCTZ triazolopyrazine core is placed in a center of the β-barrel structure, surrounded by multiple hydrophobic and aromatic residues, with the exception of few polar residues. Precisely, the side chain of R162 is in a close contact with N1-nitrogen of azaCTZ (~3.5 Å), suggesting its crucial role in a protonation step of the CEI product. Moreover, the R162 interacts with a side chain of Q12 (~2.4 Å) on one side and with a water molecule found over the triazolopyrazine core (~3.3 Å) on the other side. The position of the latter water molecule may represent the positioning of a dioxygen molecule prior it attacks CTZ-luciferin at the C2-carbon atom during monooxygenation reaction. Mechanistically, this observation suggests a cardinal dual-function role for the R162 in both the positioning of luciferin and dioxygen molecules for their interaction, and the protonating the CEI anion to secure high emission intensity. Notably, no residue that could potentially mediate initial deprotonation of the CTZ-luciferin at the N7-nitrogen or its O10H tautomer is observed, which is similar to *Renilla*-type luciferases.[21]

The R^2 6-(*para*-hydroxyphenyl) substituent is deeply anchored in the β-barrel structure, where its hydroxyl group is simultaneously hydrogen bonded by side chains of D139 (~3.3 Å), Y114 (~3.6 Å) and Y94 (~3.6 Å). The tuning of electronic state of CEI product and promoting the formation of the blue light-emitting phenolate anion is a common feature observed in structurally unrelated luciferases.[21,25] The remaining two substituents, R^1 6-(*para*-hydroxyphenyl) and R^3 8-benzyl, make predominantly hydrophobic and aromatic contacts with surrounding intra-barrel residues, with the exception of terminal hydroxyl moiety of 6-(*para*-hydroxyphenyl) substituent that forms a hydrogen bond with the backbone carbonyl of F31 (~2.6 Å).

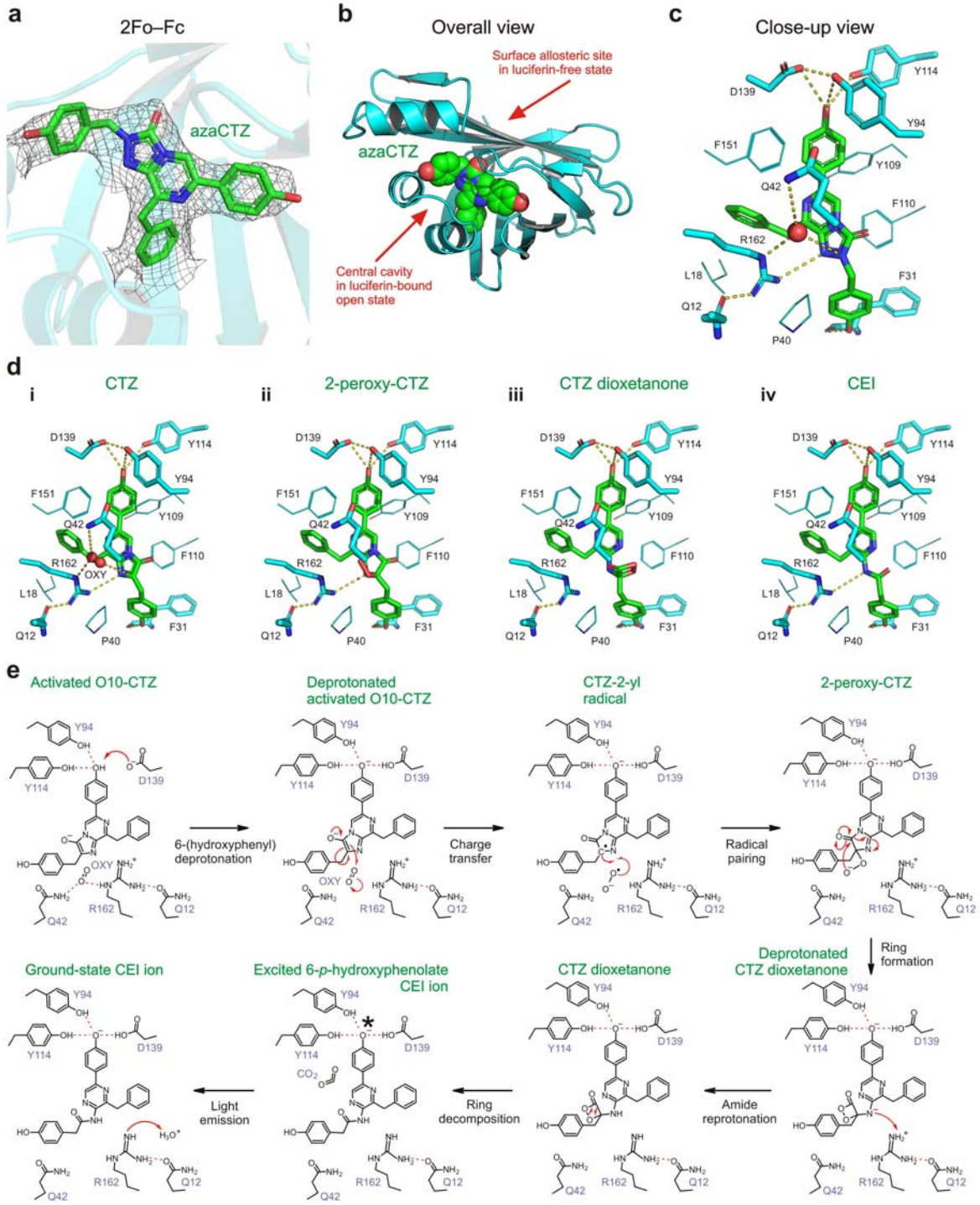

Fig. 6. Catalytic mechanism for NanoLuc-type luciferase reaction. (a) 2Fo-Fc electron density map (contour level 1.0 σ) of azaCTZ bound in the intra-barrel catalytic site of NanoLuc^{CTZ}. (b) Cartoon representation of the overall structure of NanoLuc^{CTZ} (cyan) with bound azaCTZ (green). (c) Close-up view of azaCTZ (green) bound to NanoLuc^{CTZ}, with important residues creating the active site in cyan stick representation. Red sphere; a water molecule bound in the catalytic site. Key molecular contacts are shown as dashed yellow lines. (d) Close-up views of the NanoLuc^{CTZ} active site with modelled CTZ (i), 2-peroxy-CTZ (ii), CTZ dioxetanone (iii), and CEI (iv).

Selected protein residues are shown as sticks and lines, molecular oxygen (OXY) is shown in red sphere-representation, and hydrogen bonds are shown as dashed lines. (e) A proposed mechanism for CTZ-powered NanoLuc-type luciferase reaction. CTZ enters the enzyme active site with a deprotonated imidazopyrazinone core because the pK_a of the core (7.55) is very close to the physiological pH, as demonstrated experimentally in previous work.[21] Upon the binding, the -OH group of the C6-(*p*-hydroxyphenyl) substituent is hydrogen-bonded with two tyrosines (Y94 and Y114), as well as deprotonated by D139 to form the activated dianion O10-CTZ. In the ternary Michaelis complex, the side chain of R162, and perhaps helped by the side chain of Q42, position a co-substrate molecule (dioxygen) such that it can be directly attacked by the C2 carbon of O10-CTZ. Their initial interaction occurs via a charge-transfer radical mechanism. The next step involves radical pairing and termination to form the 2-peroxy-CTZ anion, which then cyclizes via a nucleophilic addition-elimination mechanism. This step yields a highly unstable and energetic dioxetanone structure with a deprotonated amide group. At this point the amide group is protonated by R162 to avoid significant attenuation of the luminescence signal due to the formation of the deprotonated CEI product. After the protonation step, the unstable dioxetanone ring decomposes and the released energy excites the newly formed CEI product. As it returns to the ground state, the excited molecule releases a photon, representing the bioluminescence signal, together with the final products - ground-state CEI and carbon dioxide. Finally, the protonation status of R162 is restored by the proton transfer from a water molecule.

A proposal for the mechanism of NanoLuc-type catalysis

The structural information presented above allowed us to delineate a reaction mechanism for the monooxygenation of CTZ by NanoLuc-type luciferases. Co-crystal structure of azaCTZ-bound NanoLuc^{CTZ} luciferase in which substrate analogue was captured in catalytically favored conformation played a vital role in this deduction. By considering this complex structure, we were able to model the binding modes of native CTZ, the more short-lived intermediates 2-peroxy-CTZ and CTZ dioxetanone, as well as the CEI product (**Fig. 6d**). The proposed catalytic reaction mechanism is depicted schematically in **Fig. 6e**. The mechanism begins with the entry of the deprotonated form of CTZ into the β-barrel structure. We recently demonstrated that the imidazopyrazinone core of CTZ is readily deprotonated in solution because its pK_a of 7.55 is close to the physiological pH.[21] Upon binding, the -OH group of the R^2 6-(*para*-hydroxyphenyl) substituent is deprotonated by aspartate 139 to give the dianionic O10-CTZ, which affects the emission maximum of the emitted light. In the ternary Michaelis complex obtained after binding of both CTZ and molecular oxygen, the side chain of R162 helps to position the co-substrate (O_2) such that it can be directly attacked by the C2 carbon atom of the activated CTZ dianion. We propose that the initial interaction occurs via a charge-transfer mechanism, involving radical intermediates, which is analogous to *Renilla*-type reaction.[21] The next steps are radical pairing and termination to form a 2-peroxy-CTZ anion that is then cyclized via a nucleophilic addition-elimination mechanism to form a

highly unstable energetic dioxetanone structure with a deprotonated amide group. At this stage, the amide group must be protonated by R162 to ensure that luminescence occurs from the protonated form of CEI rather than the significantly less luminescent deprotonated CEI product. Following this protonation step, the unstable dioxetanone ring decomposes, and the released energy excites the newly formed CEI product. As it returns to the ground state, the excited molecule releases a photon, resulting in the bioluminescence signal. The residue R162 is then reprotonated from a water molecule (**Fig. 6e**). Finally, we think that the conformational transition from open-to-closed β-barrel structure (**Fig. 4**) may help to unload the CEI product and regenerate enzyme for a next catalytic cycle.

Molecular docking confirms two luciferin-binding sites

To further validate crystallographic structures, we performed blind molecular docking where luciferins were docked into either a monomeric or a dimeric form of the closed β-barrel NanoLuc structure (PDB ID 8AQ6). The docking poses were compared with the crystallographic FMA and CEI binding modes shown in **Fig. 2e**. The experiments with the monomeric NanoLuc have demonstrated that the luciferin molecules tend to bind in the entrance vestibule toward the central cavity, but none of the FMZ or CTZ poses was bound inside the catalytic pocket nor the allosteric site identified in our co-crystal structures (**Fig. 7a** and **Supplementary Fig. 13**). When the docking was constrained to the allosteric site, the binding energy was almost 2 kcal/mol worse, showing a higher affinity of luciferins towards the position at the β-barrel entrance vestibule above the H2 and H3 helices.

By contrast, when the homodimer NanoLuc structure was used as the receptor model, the docking results showed that there are two energetically equivalent luciferin-binding sites; the first site is in the β-barrel entrance vestibule found also in monomeric NanoLuc, and the second pose is in the surface-located allosteric site (**Fig. 7a** and **Supplementary Fig. 14**). The molecular docking thus suggests that luciferins tend to bind to the intra-barrel catalytic site but also to the allosteric site. However, the binding to the latter surface site would require the formation of the enzyme homodimer. The docking results are summarized in **Supplementary Table 3**.

Tracking the route of luciferin into the catalytic site

We then attempted docking of FMZ into the active site of different NanoLuc structures, with the closed β-barrel (PDB IDs 8AQ6, 5IBO, and 7MJB) and with the open β-barrel structures (PDB IDs: 5B0U, 8BO9, and 7VSX). The predicted binding energies differed significantly among the different structures (**Supplementary Table 4**). The docking results suggest that luciferin binding inside the intra-barrel active site of NanoLuc is favorable only in the open β-barrel conformation. At the same time, it is unlikely the luciferin could bind inside of NanoLuc with the closed β-barrel structure. Notably, the binding mode of

azaCTZ in the NanoLuc^{CTZ} crystal complex (**Fig. 6a**) was reproduced precisely by docking both FMZ and CTZ luciferins with high affinities of −11.6 and −12.2 kcal/mol, respectively (**Supplementary Fig. 15**). Thus, the docking experiments suggest that both CTZ-to-CEI and FMZ-to-FMA reactions proceed through identical conversion mechanism, as depicted in **Fig. 6e**.

Moreover, we applied adaptive steered molecular dynamics (ASMD) to probe the luciferin-binding pathway towards the intra-barrel catalytic site. We identified two hypothetical access tunnels, the first one localized between H2 and H3 helices, and the second one between H3 and H4 helices. Being pulled through the first tunnel, the simulated CTZ-luciferin ended in a similar position as the azaCTZ co-crystallized with NanoLuc^{CTZ} (**Supplementary Movies 1-3**), which was not achieved using the second tunnel. Furthermore, the luciferin was predicted to bind at the mouth of the first tunnel by molecular docking (**Fig. 7a)**, therefore, we deduce that the H2/H3 tunnel might be more relevant. Conformations of CTZ bound in the three simulated NanoLuc structures were compared to the crystal-bound conformation from the NanoLuc^{CTZ} structure. In the NanoLuc^{CTZ} luciferase, the conformation was well reproduced, while in the other structures, the poses of simulated CTZ deviated from the crystal binding mode (**Fig. 7e)**. The most prominent difference between the simulated and crystal poses is in the closed β-barrel structure, where the simulated CTZ is shifted by ~4 Å from the crystallographic mode, towards the H2 helix. This shift is likely caused by the aromatic interaction of the luciferin core with the side chain of either Y99 or F100, as observed in different replicas of the MD simulations. Moreover, unlike the open β-barrel structures, the closed NanoLuc became looser during the simulation (the distance between H2/H3 and H3/H4 increased by over 3 Å each) to enable the luciferin entry into the catalytic pocket. Interestingly, in the last phase of the NanoLuc development, which maximized the luminescence with FMZ, four mutations (L27V, K33N, K43R, and Y68D) were introduced.[8] While the R43 points toward the surface allosteric site, the other three residues are located in the region of H2, H3, and H4 helices, highlighting the functional importance of these dynamic protein elements.

A luciferin-triggered, molecular glue-like, stabilizing effect

Next, we analyzed the behavior of FMZ in monomeric and dimeric NanoLuc structures using adaptive sampling simulations with the root-mean-square deviations (RMSDs) of protein Cα-atoms as the adaptive metric, in a total simulation time of 10 μs. Markov state models (MSMs) were constructed using the RMSD of FMZ as the metric to cluster the simulations. The implied timescales plots and Chapman-Kolmogorov tests show the (**Supplementary Fig. 16**). Individual states were used to calculate kinetics and binding affinity of FMZ to the monomeric and dimeric NanoLuc. For both systems, three macrostates were constructed (**Fig. 7b**). In the monomeric form, only one macrostate described the FMZ bound in the surface allosteric site, with only about 9 % of probability (**Fig. 7c)**. Most of the time, FMZ was bound

near the H4 helix or interacted with other parts of the protein. On the other hand, in the enzyme dimeric form, two macrostates showed FMZ localized in the surface allosteric site, with more than 85% probability in total. Interestingly, FMZ had no tendency to bind into the β-barrel interior, indicating that any rearrangement of the binding site necessary for binding is not induced by the presence of the ligand near the β-barrel entrance. Finally, the kinetics and thermodynamics of the FMZ unbinding were calculated from the MSMs (**Supplementary Table 5**). The negative ΔG, high equilibrium probability (**Fig. 7c),** and lower FMZ RMSD distribution (**Supplementary Fig. 17**) indicated the strong preference of FMZ to bind to the surface allosteric site in the enzyme dimeric form, but not when it is monomeric.

The effect of the FMZ binding on the NanoLuc dimer was then analyzed by comparing adaptive sampling simulations of this dimer in the presence and absence of FMZ-luciferin. MSMs were constructed based on the RMSD of the protein Cα atoms to track the associative states of the two monomeric units, which resulted in three and four macrostates, respectively (**Supplementary Figs. 18-20**). The affinity and the equilibrium probability of the dimer when complexed with ligand show a strong stabilizing effect of FMZ on the dimeric form of NanoLuc luciferase (**Supplementary Table 6** and **Supplementary Fig. 21**). Additionally, the ASMD method was employed to simulate the dissociation of NanoLuc dimer with and without bound FMZ-luciferin (**Fig. 7d**). The potential of the mean force needed to dissociate the dimer complexed with the bound luciferin was about 10 kcal/mol higher compared to the ligand-free dimer, which implies a stabilizing effect of FMZ-luciferin on the enzyme dimer. This behavior resembles the mechanism of so-called molecular glue molecules that mediate protein-protein interactions of normally monomeric proteins.[26,27] Additionally, the X-ray structure of the NanoLuc carrying Y94A mutation, which severely compromised the luciferase activity (**Fig. 3**), was analyzed by ASMD too (**Fig. 7d**). The potential of mean force in the NanoLuc-Y94A mutant was decreased by ~25 kcal/mol compared to the dimer formed by the wild-type enzyme. The low affinity of the dimer in this mutant highlights functionally important role of the Y94 in the NanoLuc action.

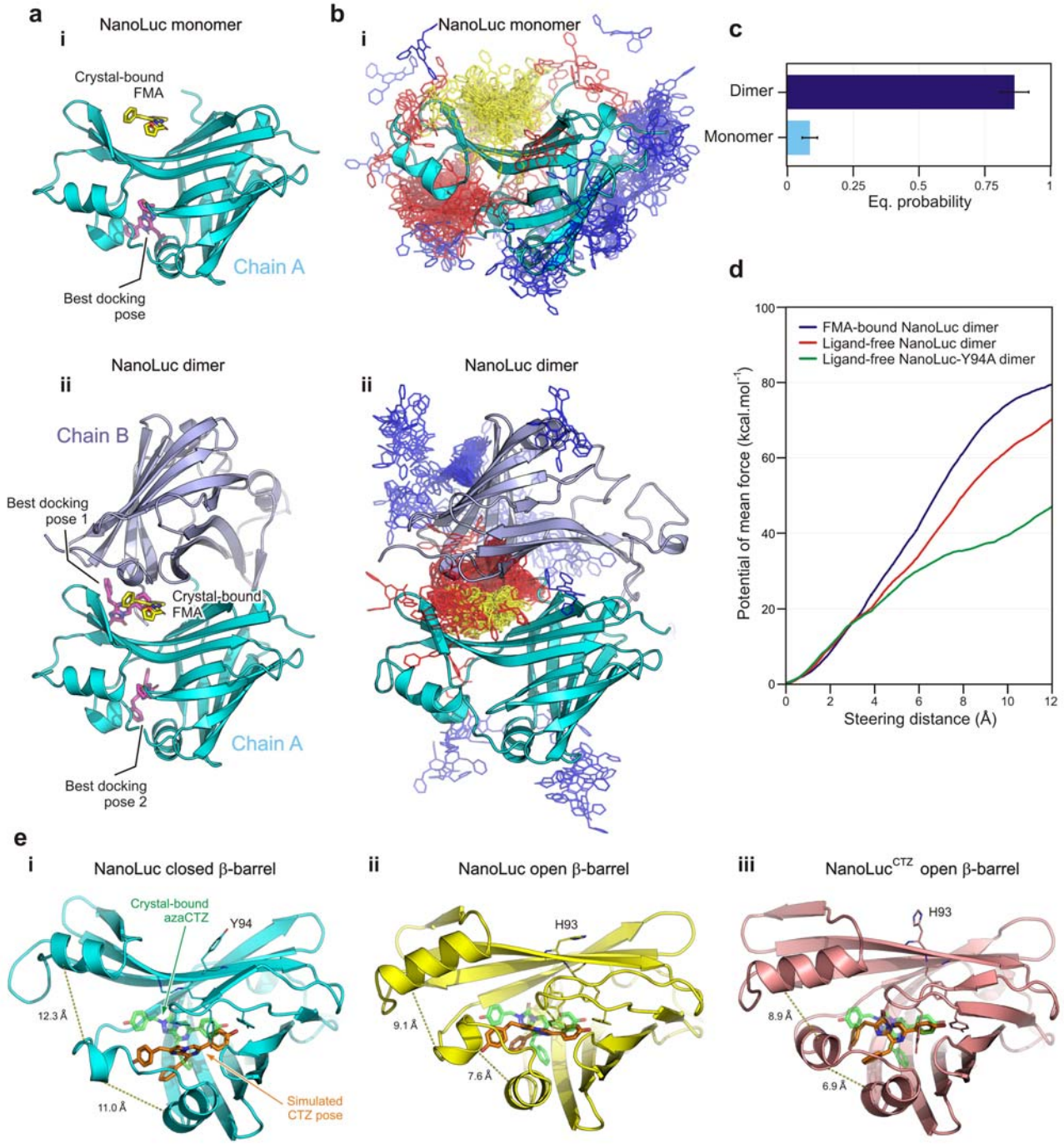

Fig. 7. Molecular docking and computational simulations of NanoLuc complexes. (a) Visualization of the best poses of FMZ (magenta sticks) from molecular docking to the NanoLuc monomer (i) and dimer (ii) (chain A cyan and chain B blue cartoon), in comparison with the crystal-bound FMA (yellow sticks). (b) Visualization of three macrostates based on the RMSD of FMZ-luciferin (yellow, red, and blue sticks in ascending order of mean RMSD values) from the adaptive sampling of NanoLuc monomer (i) and dimer (ii). In the NanoLuc monomer, the yellow macrostate was considered the bound state and the other two as unbound states, while in the dimer, the yellow and red macrostates were considered the bound states and the blue one as the unbound state. (c) Equilibrium

probabilities of FMZ macrostates bound in the surface pocket in the monomeric and dimeric NanoLuc. (d) The potential of mean force needed to steer the two subunits of different NanoLuc dimers up to 12 Å apart, obtained by adaptive steered molecular dynamics. (e) The final poses of CTZ (orange sticks) from ASMD simulations of NanoLuc structures in closed (i) and open (ii) β-barrel state, and NanoLuc^{CTZ} open β-barrel structure (iii). The crystal-bound azaCTZ (transparent green sticks) is shown in each picture for reference. The interacting aromatic residues are shown as thin sticks. The distances (in Å) between H2/H3 and H3/H4 helices are indicated by yellow dashed lines. Associated MD trajectories are shown in **Supplementary Movies 1-3**.

Discussion

Bioluminescent biosensors have a wide range of practical applications and bioassay formats. For instance, in the present COVID-19 pandemic, bioluminescent technologies play a key role in the study of the causative virus SARS-CoV-2 as well as in the development of diagnostic assays and drug development via ultrahigh-throughput screenings.[28–30] NanoLuc is the brightest known luciferase. Its light-producing activity has been used across a huge application range.[9–11,13,15] However, the molecular basis underlying its catalysis remains puzzling[8,12,17,19], and this is mainly due to the lack of structural knowledge on catalytically-favored luciferin-bound enzyme complexes.

To fill this gap, we attempted to capture luciferin-bound NanoLuc complexes through crystallographic experiments. The NanoLuc structure is formed of a 10-stranded β-barrel capped by 4 α-helices, exhibiting a structural similarity with non-catalytic FABPs, pointing toward their common evolutionary history.[17] A central intramolecular cavity is dominated by hydrophobic residues, although few polar/charged residues are also present. Therefore, it has been postulated that the luciferin should primarily bind to the central cavity inside the β-barrel structure[8,17,19], where fatty acids are typically bound in related FABPs.[31–33] Despite of this expectation, the crystal structures of NanoLuc complexed with decanoic acid (PDB IDs: 7MJB and 5IBO) showed that the fatty acid is not bound inside the β-barrel structure, but instead it occupies a pocket shaped on the protein surface. Specifically, the decanoic acid wraps around a protrusion formed by the side chain of K89. Interestingly, our initial crystallization experiments also captured luciferin molecules bound to the same surface-localized pocket, reinforcing it as a luciferin-binding allosteric site.

A question that arises is why both fatty acid and luciferin molecules tend to bind to this surface allosteric site, and not only to the central cavity endowed with catalytic function, as captured in the azaCTZ-bound NanoLuc^{CTZ} complex determined in this study. An explanation can be provided by the conformational transition between the so-called open and closed states of the β-barrel structure, which comprises several concerted structural re-arrangements, including unusual flipping of the S5 β-strand.

Previously, the open conformation of the β-barrel structure was captured in Tomabechi[17] and Inouye[19] NanoLuc structures, the latter one contains 2-(N-morpholino)ethanesulfonic acid (MES) bound inside the β-barrel. One of the major hallmarks of this open conformation is that the side chain of H93 is exposed on the surface and concomitantly the side chain of Y94, identified as a critical residue for efficient catalysis, is dipped inside the β-barrel structure, making the central cavity more voluminous. The remaining ligand-bound NanoLuc structures determined so far show the closed conformation, with the side chain of Y94 placed on the surface while the side chain of H93 is inserted in the β-barrel structure. We anticipate that the protein motions accompanying this conformational transition between the open and closed states of the β-barrel structure can be important for efficient ligand binding/unbinding events. This behavior could be somehow reminiscent to the family of small non-specific lipid transfer proteins (nsLTPs).[34,35] The nsLTPs also exhibit a central hydrophobic cavity, which is the primary lipid-binding site. However, structural studies showed that fatty acids are bound not only in the central cavity, but also on the protein surface.[34] Madni and co-workers demonstrated lipid-induced conformational changes leading to the opening of the central cavity, representing a sophisticated gating mechanism for the entry and exit of transported fatty acids.[34,35] Analogously, it is apparent that an energetic barrier of conformational transition between the open and closed states of the β-barrel structure is high, and we speculate that luciferin molecules themselves could play a role in this gating process during NanoLuc action. Mechanically, the ligand binding to the allosteric site prevents the simultaneous binding to the catalytic site, and vice versa, through concerted conformational changes, revealing the so-called homotropic negative allostery mechanism.

Another issue that should be considered carefully is the crystal packing. The NanoLuc is reported to be a monomeric enzyme[8,12], but all its crystal structures captured in the closed state of β-barrel structure display tight homotetrameric association, built up from two back-to-back homodimers. The closed state of the β-barrel structure seems to prevent the ligand binding to the intra-barrel catalytic site, but at the same time allows the binding of fatty acid or luciferin molecule into the surface-localized allosteric site. Structurally, the complexation of crystallographic NanoLuc homodimers/homotetramers having ligand bound in the surface allosteric site resembles the action mechanism of so-called molecular glue (MG) molecules.[26,27] The MG-systems are characterized by the lack of ligand binding in at least one protein partner, and an under-appreciated pre-existing low micromolar affinity between the two proteinaceous subunits that is enhanced by the ligand to reach the nanomolar range.[26] This could explain the fact that NanoLuc is monomeric enzyme when alone and in unsaturated concentration[8], but the presence of luciferin molecules may trigger its homodimerization/homotetramerization in saturated concentration to form inactive and stable enzyme-luciferin complexes, as captured in co-crystal structures. Indeed, MD simulations performed in this work imply that the presence of luciferin molecule

bound in the surface allosteric site has a positive effect on the enzyme homodimer stability. Therefore, we hypothesize that such inactive enzyme-luciferin complexes could function as a storage pool of luminescent agents *in vivo*, representing an elegant evolutionary solution to obviate the need to encode an extra luciferin-protecting protein, as described in other marine luminescent organisms.[36,37] Moreover, we identified two chloride-binding sites inside the β-barrel structure, and several additional chloride-binding sites on the enzyme surface, suggesting that chloride ions may contribute to the NanoLuc inactivation through a closing of its β-barrel structure that is accompanied by an enzyme homooligomerization, as captured in multiple crystal structures. Recently, Altamash and coworkers evidenced that elevated concentrations of chloride ions reversibly inactive NanoLuc enzyme[18], confirming this assumption. Furthermore, we previously showed that *Renilla*-type luciferases are also inhibited by halide ions[21], highlighting convergent evolution of a regulatory mechanism of marine luciferases.

It was unclear whether the binding of luciferin molecules to the surface allosteric could be the crystal lattice-biased artefact or not, and whether it has any catalytically important role. To address this concern, we performed comprehensive mutagenesis of the luciferin-binding surface pocket of NanoLuc highlighting its functional importance. The mutagenesis experiments showed substantial functional impairments when key luciferin-interacting residues were mutated, identifying Y94 as the most important residue for both FMZ and CTZ bioluminescence. Surprisingly, some mutations selectively boosted bioluminescence with CTZ-luciferin but not with FMZ-luciferin. The combined triple (D9R/H57A/K89R) mutant, termed as NanoLuc^{CTZ}, exhibited superior catalytic properties with widely accessible CTZ-luciferin ($k_{cat}/K_m = 70 \pm 7\ s^{-1}.\mu M^{-1}$), surpassing the level of catalytic efficiency of original NanoLuc/FMZ pair ($k_{cat}/K_m = 64 \pm 2\ s^{-1}.\mu M^{-1}$). Indeed, *in vivo* experiments confirmed superior CTZ-luminescence of NanoLuc^{CTZ} in HEK293T cells. Selective enhancement of bioluminescence can be explained by radically different binding modes of CTZ and FMZ in the surface allosteric pocket, as observed in our co-crystal structures. Our experiments thus evidenced an existence of a communication pathway between the allosteric and catalytic sites. Notably, we showed that restructuration of the allosteric site can dramatically enhance catalysis in the remote active site localized inside the β-barrel structure.

Recently, we showed that CTZ-to-CEI conversion proceeds via a charge-transfer radical mechanism.[21] The azaCTZ-bound NanoLuc^{CTZ} complex structure determined in this work revealed the nature of the catalytic machinery, enabling us to propose the reaction mechanism for NanoLuc-type reaction. Mechanistically, an intra-barrel R162 navigates the imidazopyrazinone component of luciferin to attack O_2 via a radical charge-transfer mechanism, as well as it protonates the excited amide product to secure high emission intensity. Previous works evidenced that the phenolate anion is the blue emitter in CTZ-bioluminescence.[21,25,38–40] For example, in *Renilla*-type luciferases, the phenolate anion of the CEI

product is generated via a deprotonation by an aspartate residue.[21] Surprisingly, similar constellation is observed in NanoLuc, where an aspartate (D139), supported by two tyrosines (Y94 and Y114), also fine-tune the electronic state of amide product, promoting the formation of the phenolate anion that emits blue photons. The aspartate mediated deprotonation of the amide product is thus a common feature employed by CTZ-utilizing marine luciferases.[21] Altogether, knowledge obtained in this study will contribute to the understanding of NanoLuc puzzling mechanism, and can be exploited for the rational design of luciferase luciferin pairs applicable in ultrasensitive bioassays and/or bio-inspired light-emitting technologies.

Methods

Luciferins and aza-luciferin analogues syntheses and characterization

The concentrated solutions of CTZ and FMZ used in this work where obtained by the hydrolysis of, respectively, hikarazines-001 and hikarazines-086 as previously described.[41] Azacoelenterazine (azaCTZ) was synthesized as described previously.[21] For azafurimazine (azaFMZ) synthesis, ^{1}H NMR and ^{13}C NMR spectra were recorded on a Bruker Avance 400 spectrometer at 400 MHz and 100 MHz, respectively. Shifts (δ) are given in ppm with respect to the TMS signal and cross-coupling constants (J) are given in Hertz. Column chromatography were performed either on Merck silica gel 60 (0.035 - 0.070 mm) or neutral alumina containing 1.5% of added water using a solvent pump and an automated collecting system driven by a UV detector set to 254 nm unless required otherwise. Sample deposition was carried out by absorption of the mixture to be purified on a small amount of the solid phase followed by its deposition of the top of the column. The low-resolution mass spectra were obtained on an Agilent 1200 series LC/MSD system using an Agilent Jet-Stream atmospheric electrospray ionization system and the high-resolution mass spectra (HRMS) were obtained using a Waters Micromass Q-Tof with an electrospray ion source.

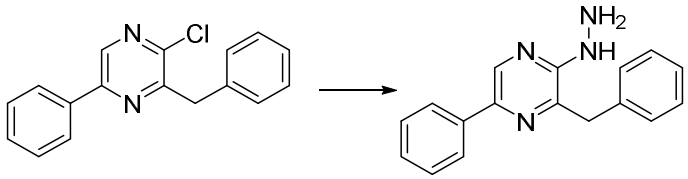

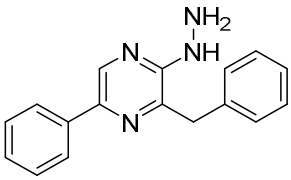

3-benzyl-2-hydrazinyl-5-phenylpyrazine: In a 20 mL sealable Biotage vial, 3-benzyl-2-chloro-5-phenylpyrazine[41] (2.0 g, 7.1 mmol) and hydrazine hydrate (1.38 mL, 28.5 mmol) were dispersed in *n*-butanol (12 mL). The vial was sealed and heated in a microwave oven at 170 °C for 8 h. The resulting mixture was dispersed in distilled water (200 mL) for 15 minutes at room temperature. The precipitated was then filtered, washed with distilled water, cyclohexane and dried under vacuum at 55°C to give the hydrazine as a yellow solid (3.71 g, 93%). ^{1}H (DMSO-d_6) δ 8.55 (s, 1H), 8.07 (s, 1H), 7.95-7.92 (m, 2 H), 7.44-7.17 (m, 9H), 4.30 (s (br), 2H), 4.12 (s, 2H). ^{13}C (DMSO-d_6) δ 153.7, 141.3, 138.8, 138.3, 137.5, 136.4, 129.5, 129.1, 128.6, 127.9, 127.2, 126.7, 125.3. HRMS (m/z): $[M+H]^+$ calcd for $C_{17}H_{16}N_4$: 277.1453, found: 277.1458.

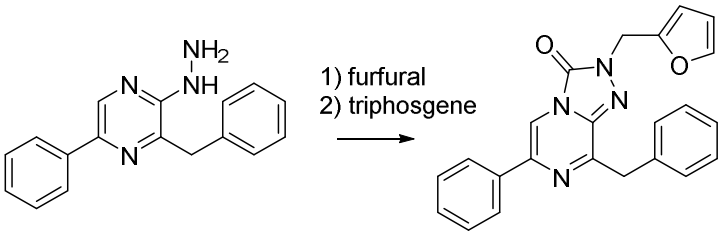

8-benzyl-2-(furan-2-ylmethyl)-6-phenyl-[1,2,4]triazolo[4,3-a]pyrazin-3(2H)-one (azafurimazine). First step: in a 250 mL round bottomed flask, 3-benzyl-2-hydrazinyl-5-phenylpyrazine (0.4 g, 1.45 mmol) and furan-2-carbaldehyde (0.12 mL, 1.45 mmol) were dispersed in acetic acid (4 mL). The mixture was stirred at room temperature during 2 minutes. The resulting solid was re-dissolved in dichloromethane (40 mL) and cyanoborohydride (0.18 g, 2.9 mmol) was added. This was stirred at room temperature for 1 h. The solution was then dispersed in water and ethyl acetate, neutralized with 1 N NaOH (1 equivalent in regard with the acetic acid added). This was extracted with ethyl acetate thrice, the organic layer was washed with a saturated solution of sodium hydrogenocarbonate, distilled water, brine and dried over $MgSO_4$. The solvent was removed under vacuum, to give the crude hydrazine (0.43 g) as a brown oil which was considered pure. Second step: under an inert atmosphere, this oil was dissolved in dry tetrahydrofuran (20 mL, dried over 4 Å molecular sieves) and solid triphosgene (0.12 g, 0.40 mmol) was added before stirring at room temperature for 40 minutes. The resulting mixture was diluted with water, extracted twice with ethyl acetate and the organic layer washed with water, brine, dried over magnesium sulfate and concentrated under vacuum to give a solid residue. A chromatography over silica gel (cyclohexane - ethyl acetate 5/1) gave a fraction containing pure azafurimazine as a yellow solid (0.37 g,

80%). ^{1}H ($CDCl_3$) δ 7.91-7.86 (m, 3H), 7.53-7.24 (m, 9H), 6.48 (dd, J = 3.3, 0.6 Hz, 1H), 6.39 (dd, J = 3.2, 1.9 Hz, 1H), 5.25 (s, 2H), 4.37 (s, 2H). ^{13}C ($CDCl_3$) δ 154.0, 148.5, 148.4, 143.0, 136.5, 136.0, 135.7, 135.5, 129.7, 128.9, 128.7, 128.5, 126.9, 125.7, 110.6, 109.5, 109.3, 43.0, 39.5. HRMS (m/z): $[M+H]^+$ calcd for $C_{23}H_{18}N_4O_2$: 383.1508, found: 383.1494.

Mutagenesis and DNA cloning

Megaprimer PCR-based mutagenesis[42] was applied to create single-point mutations as well as for gene truncation and extension. The megaprimers with the desired mutation, truncation or extension were synthesized in the first PCR reaction using a mutagenic primer and one universal primer (**Table S7**). The megaprimer was gel-purified purified by DNA electrophoresis and used as a primer in the second round of PCR to generate the complete DNA sequence with desired mutation. After PCR reaction, the original DNA template was removed by *Dpn*I treatment (2 h at 37 °C), and the mutated plasmid was transformed into chemically-competent *Escherichia coli* DH5α cells. Plasmids were isolated from three randomly selected colonies and error-free DNA genes were confirmed by DNA sequencing (Eurofins Genomics, Germany). Protein sequences of all NanoLuc variants generated and used in this work are aligned in **Supplementary Fig. 22**.

Overexpression and purification of NanoLuc luciferases

Escherichia coli BL21(DE3) cells (NEB, USA) were transformed with pET-21b plasmid encoding for N-terminally His-tagged NanoLuc gene, plated on LB-agar plates with ampicillin (100 μg/ml) and grown overnight at 37 °C. Few colonies were transferred and used to inoculate an aliquot of 10 ml of 2xLB medium containing 100 μg/ml ampicillin followed by 5-hour incubation at 37 °C. The expression of NanoLuc was induced by the addition of IPTG to a final concentration of 0.5 mM. After overnight cultivation at 20 °C, the cells were harvested by centrifugation (15 min, 4, 000 × g, 4 °C) and resuspended in a TBS buffer A (10 mM Tris-HCl, 50 mM NaCl, 20 mM imidazole, pH 7.5) containing DNase (20 μg/ml). The cells were then disrupted by sonification using Sonic Dismembrator Model 705 (Fisher Scientific, USA). The lysate was clarified by centrifugation (50 min, 21, 000 × g, 4 °C) using a Sigma 6-16K centrifuge (SciQuip, UK). The filtrated supernatant containing His-tagged NanoLuc was applied to a 5-ml Ni-NTA Superflow Cartridge (Qiagen, Germany) pre-equilibrated with TBS buffer A. NanoLuc was eluted with TBS buffer B (10 mM Tris-HCl, 50 mM NaCl pH, 250 mM imidazole, pH 7.5). Finally, NanoLuc was purified by size exclusion chromatography using Äkta Pure system (Cytiva, USA) equipped with HiLoad 16/600 Superdex 200 pg column equilibrated with a gel filtration buffer (50 mM NaCl, 10 mM Tris-HCl, pH 7.5). The protein purity was verified by SDS-PAGE. The same protocol was used for all NanoLuc variants.

Crystallization experiments

Purified NanoLuc was concentrated to a final concentration of ~10 mg/ml using Centrifugal Filter Units Amicon^{R} Ultra-15 Ultracel^{R}-3K (Merck Millipore Ltd., Ireland). Concentrated NanoLuc was mixed with a 4 molar excess of furimazine non-oxidizable analogue azaFMZ (stock solution of azaFMZ was 10 mM in isopropanol). The precipitated material was removed by centrifugation (10 min, 12,000 g, 4 °C) after 60 min incubation at 4°C, and the supernatant was directly crystallized. The crystallization was performed in Easy-Xtal 15-well crystallization plates by a hanging drop vapour diffusion, where 1 µl of NanoLuc-azafurimazine mixture was mixed with the reservoir solution (200 mM magnesium chloride, 100 mM potassium chloride, 25 mM sodium acetate pH 4.0, and 33% PEG 400) in the ratio 1:1 and equilibrated against 500 µl of the reservoir solution. The crystals usually grew in 3-5 days. The good-looking crystals were soaked overnight in the mother liquor supplemented with 10 mM FMZ or CTZ, flash-frozen in the reservoir solution supplemented with 20% glycerol by liquid nitrogen and stored for X-ray diffraction experiments. The same crystallization protocol was used for the NanoLuc Y94A mutant.

For the NanoLuc^{CTZ} co-crystallization, the purified luciferase was concentrated to a final concentration of ~10 mg/ml and mixed with a 4 molar excess of azaCTZ luciferin.[21] The crystallization was performed in Easy-Xtal 15-well crystallization plates by a hanging drop vapor diffusion, where 1 µl of NanoLuc^{CTZ}-azaCTZ mixture was mixed with the reservoir solution (100 mM ammonium acetate, 0.1 M Bis-Tris pH 5.5 mM and 17% (w/v) PEG 10000) in the ratio 1:1 and equilibrated against 500 µl of the reservoir solution. Crystals were observed at 20°C after 5-7 days. Crystals were flash-frozen in the reservoir solution supplemented with 20% glycerol by liquid nitrogen and stored for X-ray diffraction experiments. No further optimization was necessary.

Diffraction data processing and structure determinations

Diffraction data were collected at the Swiss Light Source synchrotron at the wavelength of 1.0 Å. The data were indexed and processed using XDS[43], and Aimless[3] was used for data reduction and merging. Initial phases of NanoLuc were solved by molecular replacement using Phaser[44] implemented in Phenix[45]. The structure of NanoKaz (PDB ID: 5B0U)[17] was employed as a search model for molecular replacement. Twinning was detected by phenix.xtriage[45], and taken into account during reciprocal-space refinement steps using Refmac5[46]. For the NanoLuc/FMA complex, Refmac5 refined with four twin domains and twinning operators 0.606 (h, k, l), 0.214 (h, -k, -l), 0.089 (k, h, -l) and 0.09 (-k, -h, -l). For the NanoLuc/CEI complex, there were four twin domains and twinning operators were 0.485 (h, k, l) 0.166 (-h, -k, l), 0.180 (-k, -h, -l) and 0.169 (k, h, -l). The refinement was carried out in several cycles of automated refinement in Refmac5[46] and/or phenix.refine tool[45] and manual model building performed in Coot[47]. The chemical structures and geometry restraints libraries of FMA, CEI and azaCTZ were created

using Ligand Builder and Optimization Workbench (eLBOW) implemented in Phenix[45]. The final models were validated using tools provided in Coot[47]. Structural data were graphically visualized with PyMol Molecular Graphics System (Schrödinger, LLC). Atomic coordinates and structure factors were deposited in the Protein Data Bank[20] under the ID codes: 8AQ6, 8AQI, 8AQH and 8BO9 (**Supplementary Table 1**).

Preparation of luciferin stock solutions for luminescence-measurements

Stock solutions of furimazine (Aobious, USA) and coelenterazine (Carl Roth, Germany) were prepared by dissolving a weighed amount of solid furimazine or coelenterazine in ice-cold absolute ethanol to obtain a 500 μM luciferin concentration. The stock solutions were stored in glass vials under a nitrogen atmosphere. The concentration and quality of the luciferin stock solutions were verified spectrophotometrically before each measurement.

Measurement of specific luciferase activity

Specific luciferase activity of NanoLuc and its mutants was determined at 37 °C using a FLUOStar Omega microplate reader (BMG Labtech, Germany). Buffered furimazine and coelenterazine solutions were prepared by dilution of their ethanolic stock solution into 100 mM potassium phosphate buffer (pH 7.50) to obtain a 2.2 μM concentration of luciferin. Samples of 25 μL of purified enzyme solution were placed in microplate wells. After 10 s baseline collection, the luciferase reaction was initiated by injection of 225 μL of 2.2 μM buffered furimazine or coelenterazine solution and monitored for total luminescence (240-740 nm) for 15 s. The final enzyme concentration varied between 0.03-320 nM and was tailored to each enzyme so the value of luminescence intensity immediately after reaction start and 15 s after reaction start did not vary more than 2 %. The measured specific luciferase activity was expressed in relative light units (RLU) s^{-1} M^{-1} of an enzyme. The activity of each enzyme sample was measured in at least three repetitions.

Measurement of steady-state kinetic parameters of luciferase reaction

Steady-state kinetic parameters of luciferase reaction of NanoLuc and its mutants were determined at 37 °C using a FLUOStar Omega microplate reader (BMG Labtech, Germany). Series of buffered furimazine (0.05-8.0 μM) and coelenterazine (0.05-32.0 μM) solutions were prepared by dilution of their ethanolic stock solution into 100 mM potassium phosphate buffer (pH 7.50). Samples of 25 μL of purified enzyme solution were placed in microplate wells. After 10 s baseline collection, the luciferase reaction was initiated by injection of 225 μL of buffered furimazine or coelenterazine solution and monitored for total luminescence (240-740 nm) for 15 s; this was performed for the entirety of the two

luciferin concentration series. The final enzyme concentration was chosen as 0.01 or 0.05 μM depending on the enzyme-luciferin combination, so the enzyme concentration never exceeded 1/5 of the lowest used initial luciferin concentration. To estimate the values of the Michaelis constant (K_m) of the four reactions, the obtained dependences of luciferase reaction initial velocity on the luciferin concentration were fitted by nonlinear regression to Michaelis-Menten kinetic model accounting for substrate inhibition using GraphPad Prism 8 (GraphPad Software, USA). Furthermore, the same measurement was repeated for luciferin concentration levels within the range of 0.25-4×K_m, only the luminescence of the reaction mixture was monitored either until the luminescence intensity decreased under 0.5 % of its maximal measured value (i.e. until the substrate was fully converted to product) or until the reaction has reached the 1000 s time point. In the case that for a certain enzyme-luciferin combination the luminescence never decreased under 0.5 % of its maximal measured value, an additional calibration measurement of luciferin conversion was performed using an excess of enzyme ensuring >99.5% conversion of the added luciferin. Each measurement was performed in at least three repetitions.

Monitoring the luciferase reaction beyond the initial linear phase up to complete conversion of the substrate allows for the determination of its kinetic constants from reaction rate time progress in relative units without the need for luminometer quantum yield calibration.[3] The measured dependences of luminescence intensity on the reaction time were transformed into cumulative luminescence in time. The obtained conversion curves capturing the initial reaction velocity and total luciferin conversion were globally fitted by numerical methods using the KinTek Explorer[48] (KinTek Corporation, USA) to directly obtain the values of turnover number k_{cat}, Michaelis constant K_m, specificity constant k_{cat}/K_m, and equilibrium dissociation constant for enzyme-product complex K_p and enzyme-substrate-substrate complex K_s according to models (**Scheme 1**) for NanoLuc and (**Scheme 2**) for its Y94A mutant. To reflect fluctuation in experimental data, the values of substrate or enzyme concentrations were corrected (±5%) to obtain best fits. Residuals were normalized by sigma value for each data point. In addition to S.E. values, a more rigorous analysis of the evaluation reliability was performed by confidence contour analysis using FitSpace Explorer[49] (KinTek Corporation, USA). The scaling factor, relating the luminescence signal to product concentration, was applied as one of the fitted parameters, well defined by the end state of total conversion curves. Depletion of the available substrate after the reaction was verified by repeated injection of a fresh enzyme, resulting in no or negligible luminescence.

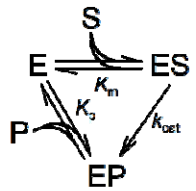

(Scheme 1)

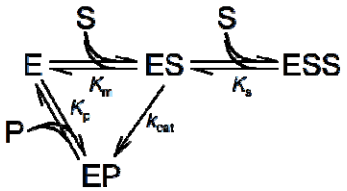

(Scheme 2)

Live-cell imaging assays

ARPE-19 cell line was cultured in Knockout Dulbecco's modified Eagle's medium (Invitrogen, Life Technologies Ltd.) containing 10% foetal bovine serum (FBS), (Biosera), 1x GlutaMAX (Invitrogen, Life Technologies Ltd.), 1 × MEM non-essential amino acid solution, 1 × penicillin/streptomycin (Biosera) and 10 μM β mercaptoethanol (Sigma-Aldrich). The cells were incubated at 37 °C/5 % CO_2 and regularly passaged using trypsin.

Lentiviral particles were generated as described previously.[50,51] Briefly, HEK293T cells were transfected with pSIN vector coding for either NanoLuc^{CTZ} or NanoLuc gene together with 2nd generation of lentiviral production plasmids psPAX2 (Addgene #12260) and pMD2.G (Addgene #12259) kindly provided by Didier Trono. After transfection, the cell culture medium was exchanged for medium containing: OptiMEM (Invitrogen, Life Technologies Ltd.), 1% FBS, 1% MEM non-essential amino acid solution, 1% penicillin/streptomycin) and was collected every 12 hours for a total of 48 hours. Virus supernatant was centrifuged (4.500 × g, 10 minutes, room temperature), filtered through a 0.45 μm low protein-binding filter. The supernatant was mixed with Polybrene (Sigma-Aldrich) at final concentration of 5 μg/ml and applied to cells overnight. The next day, the culture medium containing viral particles was replaced with a fresh medium. Transduced cells were then cultured in the presence 1 μg/ml puromycin.

For luciferase activity measurements, cells were seeded onto a 40 mm cell culture petri dish, allowed to adhere and recover for 16 hours. Cell culture medium was replaced with pre-heated (37 °C) fresh medium containing EnduRen (60 μM) or 1x Nano-Glo Endurazine (Promega). Luciferase activity was measured using LuminoCell device, as described previously.[24]

Preparation of ligand molecules for docking

The structures of the ligands were prepared using Avogadro 1.2.0 software.[52] The multiplicity of the bonds was edited to match the keto forms of FMZ and CTZ, all missing hydrogens were added, and then the structures were minimized by the steepest descend algorithm in the Auto Optimize tool of Avogadro, using the Universal Force Field (UFF). Next, the ligands were uploaded to the RESP ESP charge Derive (R.E.D.) Server *Development* 2.0[53] to derivate the restrained electrostatic potential (RESP) charges. Then, AutoDock atom types were added and PDBQT files were generated by MGLTools[54,55].

Preparation of receptor molecules for docking

The NanoLuc structures, which served as receptors for docking (PDB IDs 8AQ6, 8BO9, 5IBO, 5B0U, 7MJB), were downloaded from the RCSB PDB[56], aligned to PDB ID 8AQ6 in PyMOL 1.8.4[57], and stripped of all non-protein atoms. The structures were protonated with H++ web server v. 4.0[58,59], using pH = 7.4, salinity = 0.1 M, internal dielectric = 10, and external dielectric = 80 as parameters. AutoDock atom types and Gasteiger charges were added to the receptors by MGLTools[54,55] and the corresponding PDBQT files were generated. All receptors were prepared without ligands.

Molecular docking

The AutoDock Vina 1.1.2[60] algorithm was used for molecular docking. For site-directed docking to the crystallographic binding pocket, the docking grid was selected to be x = 32 Å, y = 22 Å, z = 30 Å sized box with a center in x = 40, y = −47, z = 62 for NanoLuc monomer and a 30 × 24 × 40 Å box with a center in (35,−50,60) for NanoLuc dimer covering the catalytic pocket, which was computed with HotSpot Wizard 3.1[61]. For blind docking, a 60 × 50 × 46 Å box with a center in (47,−57,63) covering the whole protein was used for the monomer, and a 65 × 75 × 50 Å box with a center in (44,−44,62) for the dimer. For site-directed docking to the beta-barrel, five different-sized docking grids were used: four cubic boxes with a side of 22, 20, 18, and 12 Å centered in (47, −60,62), and another 16 × 16 × 18 Å sized box with a center in (49,−60, 62). The flag --exhaustiveness = 100 was used to sample the possible conformational space thoroughly. The number of output conformations of the docked ligand was set to 10. The results were analyzed in PyMOL 1.8.4 software[57].

Ligand preparation for adaptive sampling

The structures of the ligands (FMZ and Cl^-) were extracted from the NanoLuc crystal structure. The multiplicity of bonds in the FMZ structure was adjusted to match the keto form and all missing hydrogens were added using Avogadro 1.2.0 software[62]. The *antechamber* module of AmberTools16[63] was used to calculate the charges for the ligands, add the atom types of the Amber force field and compile them in a

PREPI parameters file. Also, the *parmchk2* tool from AmberTools16 was used to create an additional FRCMOD parameter file for FMZ to compensate for any missing parameters.

System preparation and equilibration

The structure of the NanoLuc monomer was extracted from the crystallographic structure of the NanoLuc dimer in a complex with FMZ. The crystallographic water molecules were kept in the system. Three starting NanoLuc systems were prepared: (i) monomer + FMZ + two O_2 molecules, (ii) dimer + two O_2 molecules, and (iii) dimer + FMZ + two O_2 molecules.

The following steps were performed with the High Throughput Molecular Dynamics (HTMD)[64] scripts. Each protein structure was protonated with PROPKA 2.0 at pH 7.5[65]. For the systems with FMZ, one molecule was placed in the same site as in the initial crystal structure. The three systems were solvated in a cubic water box of TIP3P[66] water molecules with the edges at least 10 Å away from the protein, by the *solvate* module of HTMD. Cl^- and Na^+ ions were added to neutralize the charge of the protein and get a final salt concentration of 0.1 M. The topology of the system was built, using the *amber.build* module of HTMD, with the ff14SB[67] Amber force field and the previously compiled PREPI and FRCMOD parameter files for the ligands. The systems were equilibrated using the *equilibration_v2* module of HTMD[64]. The system was first minimized using a conjugate-gradient method for 500 steps. Then the system was heated to 310 K and minimized as follows: (i) 500 steps (2 ps) of NVT thermalization with the Berendsen barostat with 1 $kcal \cdot mol^{-1} \cdot Å^{-2}$ constraints on all heavy atoms of the protein, (ii) 1,250,000 steps (5 ns) of NPT equilibration with Langevin thermostat and same constraints, and (iii) 1,250,000 steps (5 ns) of NPT equilibration with the Langevin thermostat without any constraints. During the equilibration simulations, holonomic constraints were applied on all hydrogen-heavy atom bond terms, and the mass of the hydrogen atoms was scaled with factor 4, enabling 4 fs time steps[68–71]. The simulations employed periodic boundary conditions, using the particle mesh Ewald method for treatment of interactions beyond 9 Å cut-off, electrostatic interactions suppressed for more than 4 bond terms away from each other, and the smoothing and switching van der Waals and electrostatic interaction cut-off at 7.5 Å.[70]

Adaptive sampling

HTMD[64] was used to perform adaptive sampling of the conformations of the three NanoLuc systems (dimer + FMZ + 2 O_2, dimer + 2 O_2, monomer + FMZ + 2 O_2). Fifty ns production MD runs were started with the systems that resulted from the equilibration cycle and employed the same settings as the last step of the equilibration. The trajectories were saved every 0.1 ns. Adaptive sampling was performed using, as

the adaptive metric, the root-mean-square deviation (RMSD) of all Cα atoms of the protein against the crystal structure as a reference, and time-lagged independent component analysis (tICA)[72] projection in 1 dimension. 20 epochs of 10 parallel MDs were performed for the two systems with NanoLuc dimer, corresponding to a cumulative time of 10 µs per system. For the monomer, 29 epochs of 10 MDs were calculated with the same metric (14.5 µs), and additional 4 epochs of 10 MDs (2 µs) were calculated with the contacts metric between all heavy atoms of FMZ and residues 41I, 57H, and 89K located in the active site of the protein.

Markov state model construction

The simulations were made into a simulation list using HTMD[64], the water and ions were filtered out, and unsuccessful simulations shorter than 50 ns were omitted. Such filtered trajectories were combined for each system, which resulted in 10 µs of cumulative simulation time for the two systems with NanoLuc dimer and 16.5 µs for the system with NanoLuc monomer. The ligand unbinding dynamics of the systems with FMZ were studied by the RMSD metric for the heavy atoms of FMZ against the initial position of FMZ in the system. The data were clustered using the MiniBatchKmeans algorithm to 1000 clusters. For the NanoLuc dimer with FMZ, a 20 ns lag time was used in the models to construct three Markov states, while for the monomer with FMZ 3 Markov states were constructed using a 30 ns lag time.The dimer dissociation dynamics of the dimer systems were studied by the same metric used in the adaptive sampling – the RMSD of the Cα atoms of the protein. The data were clustered using the MiniBatchKmeans algorithm to 1000 clusters. For NanoLuc dimer with FMZ, a 20 ns lag time was used in the models to construct 3 Markov states, while for dimer alone, 4 Markov states were constructed using a 20 ns lag time. The Chapman-Kolmogorov test was performed to assess the quality of all the constructed states. The states were visualized in VMD 1.9.3[73] and statistics of the RMSD value for each state were calculated (mean RMSD, SD, minimum RMSD, and maximum RMSD). The trajectory was saved for each model.

Calculation of kinetics

Kinetic values (MFPT on/off, k_{on}, k_{off}, ΔG^0_{eq}, and K_D) were calculated by the *kinetics* module of HTMD[64] between the source state and the sink state. In the FMZ unbinding analysis, the source state was defined as the unbound state of FMZ and the sink state as the bound state, while in the dimer dissociation analysis, the source state was defined as the most dissociated state and sink as the associated state. Also, the equilibrium population of each macrostate was calculated and visualized. Finally, bootstrapping of the

kinetics analysis was performed, using randomly selected 80 % of the data, run 100 times. The kinetic values were then averaged, and the standard deviations were calculated.

Preparation and minimization of NanoLuc dimers for ASMD

The crystal structures of three different NanoLuc dimers were studied: (i) an asymmetric dimer with bound FMZ, (ii) a symmetric dimer of NanoLuc-Y94A mutant, and (iii) a symmetric NanoLuc-R164Q mutant (PDB ID 7MJB). First, the structures were stripped of all non-protein atoms. Next, the structures were protonated with the H++ web server v. 4.0[58,59], using pH = 7.4, salinity = 0.1 M, internal dielectric = 10, and external dielectric = 80 as parameters. Then the crystallographic water molecules were added to the systems. Next, histidine residues were renamed according to their protonation state (HID – Nδ protonated, HIE – Nε protonated, HIP – both Nδ and Nε protonated). The FMZ ligand was prepared as described in Ligand preparation for adaptive sampling above. Moreover, it was minimized by the steepest descend algorithm in the Auto Optimize tool of Avogadro 1.2.0[62], using the Universal Force Field (UFF). In the case of the asymmetric dimer, two systems were prepared – one with FMZ and one without, while the symmetric NanoLuc dimers were prepared without FMZ, yielding four systems in total. The *tLEaP* module of AmberTools16[74] was used to neutralize the systems with Cl^- and Na^+ ions, import the ff14SB force field[75] to describe the protein and the FMZ parameters to describe the ligand, add an octahedral box of TIP3P water molecules[76] to the distance of 20 Å from any atom in the system, and generate the topology file, coordinate file, and PDB file. All crystallographic water molecules that were overlapping with the protein or FMZ were removed from the input PDB file and *tLEaP* was rerun.

The system equilibration was carried out with the *PMEMD.CUDA*[77–79] module of Amber 16[74]. In total, five minimization steps and twelve steps of equilibration dynamics were performed. The first four minimization steps were composed of 2,500 cycles of the steepest descent algorithm followed by 7,500 cycles of the conjugate gradient algorithm each, while gradually decreasing harmonic restraints. The restraints were applied as follows: 500 $kcal \cdot mol^{-1} \cdot Å^{-2}$ on all heavy atoms of the protein, and then 500, 125, and 25 $kcal \cdot mol^{-1} \cdot Å^{-2}$ on backbone atoms only. The fifth step was composed of 5,000 cycles of the steepest descent algorithm followed by 15,000 cycles of the conjugate gradient algorithm without any restraint.

The equilibration MD simulations consisted of twelve steps: (i) first step involved 20 ps of gradual heating from 0 to 310 K at constant volume using Langevin dynamics, with harmonic restraints of 200 $kcal \cdot mol^{-1} \cdot Å^{-2}$ on all heavy atoms of the protein, (ii) ten steps of 400 ps equilibration Langevin dynamics each at a constant temperature of 310 K and a constant pressure of 1 bar with decreasing harmonic restraints of 150, 100, 75, 50, 25, 15, 10, 5, 1, and 0.5 $kcal \cdot mol^{-1} \cdot Å^{-2}$ on backbone atoms of the proteins, and (iii) the last step involving 400 ps of equilibration dynamics at a constant temperature of

310 K and a constant pressure of 1 bar with no restraint. The simulations employed periodic boundary conditions based on the particle mesh Ewald method[80] for treatment of the long-range interactions beyond the 10 Å cut-off, the SHAKE algorithm[81] to constrain the bonds that involve hydrogen atoms, and the Langevin temperature equilibration using a collision frequency of 1 ps^{-1}. After the equilibration, the number of Cl^- and Na^+ ions needed to reach 0.1 M salinity was calculated using the average volume of the system in the last equilibration step. The whole process was repeated, from the *tLEaP* step, to correct the number of the added ions.

Adaptive steered molecular dynamics

The dimer dissociation trajectories were calculated with adaptive steered molecular dynamics (ASMD). The ASMD method applies constant external force on two atoms in the simulated systems. This can be used to either push two atoms from each other or pull them together to simulate unbinding/binding of ligands or dissociation/association of proteins. During ASMD, several parallel simulations are started from the same state. The simulation runs in stages where a chosen value changes the distance between selected atoms. At the end of each stage, the parallel simulations are collected and analyzed, and the Jarzynski average is calculated. The trajectory with its work value closest to the average is selected and the state at the end of this trajectory is used as the starting point for the next stage. For our purpose, we use the default values for setting up ASMD which were found in the tutorial for AMBER and the ASMD publication[82]. The simulations were run with 25 parallel MDs, steered by 2 Å stages of distance increments, with a velocity of 10 Å/ns, and a force of 7.2 N. The rest of the MD settings were set as in the last equilibration step. The atoms selected for steering were Cα atoms from Ile58 residues. The selected Cα atoms are from the dimer interface residues so that the two subunits could be pushed apart. This residue is a part of a β-barrel structure, which makes it suitable for steering since the structure is relatively rigid. The distance between the two Cα atoms was measured using Measurement Wizard in PyMOL[57]. The two subunits were steered apart for additional 20 Å. MD trajectories were analyzed and visualized in PyMOL[57] using the smooth function and exported as movie (.mpg) files.

Author Contributions

M.N., D.P. and J.H. contributed equally to this study. N.M., T.S., J.T., V.N. prepared and cloned the DNA constructs, and produced the protein samples for crystallization and biochemical experiments. R.B., G.G., Y.L.J. synthetized the luciferin molecules. M.N. carried out the crystallization screenings, and optimized crystallization hits. M.N. and M.M. collected diffraction data and solved the protein crystal structures. D.P., T.S., M.M., Z.P. performed luminescence measurements and kinetic analyses. T.B.

engineered stable mammalian cell lines and performed cell-based bioluminescence experiments. J.H., S.M.M., J.D. and D.B. carried out computational and theoretical experiments and MD simulations. M.M., Y.L.J., Z.P., J.D., M.T., D.B. and Z.P. designed the project, supervised research and interpreted data. M.N. and M.M. wrote the manuscript with contributions from all authors. All authors have approved the final version of the manuscript.

Data availability

The authors declare no competing financial interest. Atomic coordinates and structural factors have been saved in the Protein Data bank (www.wwpdb.org)[20] under PDB ID accession codes: 8AQH, 8AQI, 8AQ6 and 8BO9. The authors will release the atomic coordinates and experimental data upon article publication.

Competing interest statements

The authors declare no competing interests.

Acknowledgements

The authors would like to express their thanks to the Czech Science Foundation (GA22-09853S) and the Czech Ministry of Education (INBIO CZ.02.1.01/0.0/0.0/16_026/0008451, RECETOX RI LM2018121, e-INFRA LM2018140). This project has received funding from the European Union's Horizon 2020 research and innovation program under grant agreement No 857560 (CETOCOEN Excellence) and No 814418 (Sinfonia). This publication reflects only the author's view, and the European Commission is not responsible for any use that may be made of the information it contains. M. T. is a Brno Ph.D. Talent Scholarship holder funded by the Brno City Municipality. CIISB research infrastructure project (LM2018127) is acknowledged for financial support of the measurements at Biomolecular Interactions and Crystallization Core Facility. G.G. acknowledges a PhD fellowship from the Université Paris Descartes, Sorbonne Paris Cité, France and we also benefited from the Valoexpress funding calls of the Institut Pasteur, Paris. The crystallographic data were collected at the PXIII beamline at the Swiss Light Source (SLS) in Villigen (Switzerland). We are grateful to the members of the SLS synchrotron for the use of their beamline and help during data collection. We thank Dr. Andrea Smith for help during X-ray data collection.

References

1. Haddock, S. H. D., Moline, M. A. & Case, J. F. Bioluminescence in the sea. *Ann Rev Mar Sci* **2**, 443–493 (2010).
2. Mitiouchkina, T. *et al.* Plants with genetically encoded autoluminescence. *Nat Biotechnol* **38**, 944–946 (2020).
3. Schenkmayerova, A. *et al.* Engineering the protein dynamics of an ancestral luciferase. *Nat Commun* **12**, 3616 (2021).
4. Su, Y. *et al.* Novel NanoLuc substrates enable bright two-population bioluminescence imaging in animals. *Nat Methods* **17**, 852–860 (2020).
5. Syed, A. J. & Anderson, J. C. Applications of bioluminescence in biotechnology and beyond. *Chem Soc Rev* **50**, 5668–5705 (2021).
6. Shimomura, O., Masugi, T., Johnson, F. H. & Haneda, Y. Properties and reaction mechanism of the bioluminescence system of the deep-sea shrimp Oplophorus gracilorostris. *Biochemistry* **17**, 994–998 (1978).
7. Inouye, S., Watanabe, K., Nakamura, H. & Shimomura, O. Secretional luciferase of the luminous shrimp Oplophorus gracilirostris: cDNA cloning of a novel imidazopyrazinone luciferase. *FEBS Lett* **481**, 19–25 (2000).
8. Hall, M. P. *et al.* Engineered Luciferase Reporter from a Deep Sea Shrimp Utilizing a Novel Imidazopyrazinone Substrate. *ACS Chem Biol* **7**, 1848–1857 (2012).
9. Guo, Z. *et al.* Engineering and exploiting synthetic allostery of NanoLuc luciferase. *Nat Commun* **13**, 789 (2022).
10. England, C. G., Ehlerding, E. B. & Cai, W. NanoLuc: A Small Luciferase Is Brightening Up the Field of Bioluminescence. *Bioconjug Chem* **27**, 1175–1187 (2016).
11. Biewenga, L., Rosier, B. J. H. M. & Merkx, M. Engineering with NanoLuc: a playground for the development of bioluminescent protein switches and sensors. *Biochem Soc Trans* **48**, 2643–2655 (2020).

12. Dixon, A. S. *et al.* NanoLuc Complementation Reporter Optimized for Accurate Measurement of Protein Interactions in Cells. *ACS Chem Biol* **11**, 400–408 (2016).
13. Yeh, H.-W. *et al.* Red-shifted luciferase-luciferin pairs for enhanced bioluminescence imaging. *Nat Methods* **14**, 971–974 (2017).
14. Yeh, H.-W. *et al.* ATP-Independent Bioluminescent Reporter Variants To Improve in Vivo Imaging. *ACS Chem Biol* **14**, 959–965 (2019).
15. Nagai, T. & Hattori, M. Tiny but bright. *Nat Rev Chem* 1–2 (2022) doi:10.1038/s41570-022-00413-6.
16. Shipunova, V. O., Shilova, O. N., Shramova, E. I., Deyev, S. M. & Proshkina, G. M. A Highly Specific Substrate for NanoLUC Luciferase Furimazine Is Toxic in vitro and in vivo. *Russ J Bioorg Chem* **44**, 225–228 (2018).
17. Tomabechi, Y. *et al.* Crystal structure of nanoKAZ: The mutated 19 kDa component of Oplophorus luciferase catalyzing the bioluminescent reaction with coelenterazine. *Biochem Biophys Res Commun* **470**, 88–93 (2016).
18. Altamash, T., Ahmed, W., Rasool, S. & Biswas, K. H. Intracellular Ionic Strength Sensing Using NanoLuc. *Int J Mol Sci* **22**, 677 (2021).
19. Inouye, S. *et al.* Reverse mutants of the catalytic 19 kDa mutant protein (nanoKAZ/nanoLuc) from Oplophorus luciferase with coelenterazine as preferred substrate. *PLoS One* **17**, e0272992 (2022).
20. Berman, H. M. *et al.* The Protein Data Bank. *Nucleic Acids Res* **28**, 235–242 (2000).
21. Schenkmayerova, A. *et al.* A catalytic mechanism for Renilla-type bioluminescence. 2022.02.09.479090 Preprint at https://doi.org/10.1101/2022.02.09.479090 (2022).
22. Krissinel, E. & Henrick, K. Inference of macromolecular assemblies from crystalline state. *J Mol Biol* **372**, 774–797 (2007).
23. Kayikci, M. *et al.* Visualization and analysis of non-covalent contacts using the Protein Contacts Atlas. *Nat Struct Mol Biol* **25**, 185–194 (2018).

24. Weissová, K. *et al.* LuminoCell: a versatile and affordable platform for real-time monitoring of luciferase-based reporters. *Life Sci Alliance* **5**, e202201421 (2022).

25. Loening, A. M., Wu, A. M. & Gambhir, S. S. Red-shifted Renilla reniformis luciferase variants for imaging in living subjects. *Nat Methods* **4**, 641–643 (2007).

26. Cao, S. *et al.* Defining molecular glues with a dual-nanobody cannabidiol sensor. *Nat Commun* **13**, 815 (2022).

27. Schreiber, S. L. The Rise of Molecular Glues. *Cell* **184**, 3–9 (2021).

28. Elledge, S. K. *et al.* Engineering luminescent biosensors for point-of-care SARS-CoV-2 antibody detection. *Nat Biotechnol* **39**, 928–935 (2021).

29. Azad, T. *et al.* Luciferase-Based Biosensors in the Era of the COVID-19 Pandemic. *ACS Nanosci. Au* **1**, 15–37 (2021).

30. Mathieu, C. *et al.* A Bioluminescent 3CLPro Activity Assay to Monitor SARS-CoV-2 Replication and Identify Inhibitors. *Viruses* **13**, 1814 (2021).

31. Zanotti, G., Scapin, G., Spadon, P., Veerkamp, J. H. & Sacchettini, J. C. Three-dimensional structure of recombinant human muscle fatty acid-binding protein. *J Biol Chem* **267**, 18541–18550 (1992).

32. Young, A. C. *et al.* Structural studies on human muscle fatty acid binding protein at 1.4 A resolution: binding interactions with three C18 fatty acids. *Structure* **2**, 523–534 (1994).

33. Matsuoka, S. *et al.* Water-mediated recognition of simple alkyl chains by heart-type fatty-acid-binding protein. *Angew Chem Int Ed Engl* **54**, 1508–1511 (2015).

34. Madni, Z. K., Tripathi, S. K. & Salunke, D. M. Structural insights into the lipid transfer mechanism of a non-specific lipid transfer protein. *Plant J* **102**, 340–352 (2020).

35. Madni, Z. K., Kumar, A., Kumar, U., Jaiswal, D. & Salunke, D. M. Dynamics of lipid displacement inside the hydrophobic cavity of a nonspecific lipid transfer protein from Solanum melongena. *J Biomol Struct Dyn* 1–11 (2022) doi:10.1080/07391102.2022.2097956.

36. Titushin, M. S. *et al*. Coelenterazine-binding protein of Renilla muelleri: cDNA cloning, overexpression, and characterization as a substrate of luciferase. *Photochem Photobiol Sci* **7**, 189–196 (2008).

37. Titushin, M. S., Feng, Y., Lee, J., Vysotski, E. S. & Liu, Z.-J. Protein-protein complexation in bioluminescence. *Protein Cell* **2**, 957–972 (2011).

38. Liu, Z.-J. *et al.* Crystal structure of obelin after Ca2+-triggered bioluminescence suggests neutral coelenteramide as the primary excited state. *PNAS* **103**, 2570–2575 (2006).

39. Imai, Y. *et al.* Fluorescence properties of phenolate anions of coelenteramide analogues: the light-emitter structure in aequorin bioluminescence. *Journal of Photochemistry and Photobiology A: Chemistry* **146**, 95–107 (2001).

40. Li, Z.-S., Zhao, X., Zou, L.-Y. & Ren, A.-M. The dynamics simulation and quantum calculation investigation about luminescence mechanism of coelenteramide. *Photochem Photobiol* **89**, 849–855 (2013).

41. Coutant, E. P. *et al*. Gram-scale synthesis of luciferins derived from coelenterazine and original insights into their bioluminescence properties. *Org. Biomol. Chem.* **17**, 3709–3713 (2019).

42. Sarkar, G. & Sommer, S. S. The ‘megaprimer’ method of site-directed mutagenesis. *Biotechniques* **8**, 404–407 (1990).

43. Kabsch, W. XDS. *Acta Crystallogr D Biol Crystallogr* **66**, 125–132 (2010).

44. McCoy, A. J. *et al.* Phaser crystallographic software. *J Appl Crystallogr* **40**, 658–674 (2007).

45. Liebschner, D. *et al.* Macromolecular structure determination using X-rays, neutrons and electrons: recent developments in Phenix. *Acta Crystallogr D Struct Biol* **75**, 861–877 (2019).

46. Murshudov, G. N. *et al.* REFMAC5 for the refinement of macromolecular crystal structures. *Acta Crystallogr D Biol Crystallogr* **67**, 355–367 (2011).

47. Emsley, P., Lohkamp, B., Scott, W. G. & Cowtan, K. Features and development of Coot. *Acta Crystallogr D Biol Crystallogr* **66**, 486–501 (2010).

48. Johnson, K. A., Simpson, Z. B. & Blom, T. Global kinetic explorer: a new computer program for dynamic simulation and fitting of kinetic data. *Anal Biochem* **387**, 20–29 (2009).

49. Johnson, K. A., Simpson, Z. B. & Blom, T. FitSpace explorer: an algorithm to evaluate multidimensional parameter space in fitting kinetic data. *Anal Biochem* **387**, 30–41 (2009).

50. Peskova, L. *et al.* miR-183/96/182 cluster is an important morphogenetic factor targeting PAX6 expression in differentiating human retinal organoids. *Stem Cells* (2020) doi:10.1002/stem.3272.

51. Peskova, L., Cerna, K., Oppelt, J., Mraz, M. & Barta, T. Oct4-mediated reprogramming induces embryonic-like microRNA expression signatures in human fibroblasts. *Sci Rep* **9**, 15759 (2019).

52. Hanwell, M. D. *et al.* Avogadro: an advanced semantic chemical editor, visualization, and analysis platform. *J Cheminform* **4**, 17 (2012).

53. Vanquelef, E. *et al.* R.E.D. Server: a web service for deriving RESP and ESP charges and building force field libraries for new molecules and molecular fragments. *Nucleic Acids Res* **39**, W511-517 (2011).

54. Sanner, M. F. Python: a programming language for software integration and development. *J Mol Graph Model* **17**, 57–61 (1999).

55. Sanner, M. F., Olson, A. J. & Spehner, J. C. Reduced surface: an efficient way to compute molecular surfaces. *Biopolymers* **38**, 305–320 (1996).

56. Burley, S. K. *et al.* RCSB Protein Data Bank: powerful new tools for exploring 3D structures of biological macromolecules for basic and applied research and education in fundamental biology, biomedicine, biotechnology, bioengineering and energy sciences. *Nucleic Acids Research* **49**, D437–D451 (2021).

57. The PyMOL Molecular Graphics System, v. 1.8.4.

58. Anandakrishnan, R., Aguilar, B. & Onufriev, A. V. H++ 3.0: automating pK prediction and the preparation of biomolecular structures for atomistic molecular modeling and simulations. *Nucleic Acids Research* **40**, W537–W541 (2012).

59. Gordon, J. C. *et al.* H++: a server for estimating pKas and adding missing hydrogens to macromolecules. *Nucleic Acids Res* **33**, W368–W371 (2005).

60. Trott, O. & Olson, A. J. AutoDock Vina: improving the speed and accuracy of docking with a new scoring function, efficient optimization and multithreading. *J Comput Chem* **31**, 455–461 (2010).

61. Sumbalova, L., Stourac, J., Martinek, T., Bednar, D. & Damborsky, J. HotSpot Wizard 3.0: web server for automated design of mutations and smart libraries based on sequence input information. *Nucleic Acids Research* **46**, W356–W362 (2018).

62. Hanwell, M. D. *et al.* Avogadro: an advanced semantic chemical editor, visualization, and analysis platform. *Journal of Cheminformatics* **4**, 17 (2012).

63. Case, D. A. *et al.* AMBER 16. (2016).

64. Doerr, S., Harvey, M. J., Noé, F. & De Fabritiis, G. HTMD: High-Throughput Molecular Dynamics for Molecular Discovery. *J. Chem. Theory Comput.* **12**, 1845–1852 (2016).

65. Bas, D. C., Rogers, D. M. & Jensen, J. H. Very fast prediction and rationalization of pKa values for protein-ligand complexes. *Proteins* **73**, 765–783 (2008).

66. Jorgensen, W., Chandrasekhar, J., Madura, J., Impey, R. & Klein, M. Comparison of Simple Potential Functions for Simulating Liquid Water. *J. Chem. Phys.* **79**, 926–935 (1983).

67. Maier, J. A. *et al.* ff14SB: Improving the Accuracy of Protein Side Chain and Backbone Parameters from ff99SB. *J. Chem. Theory Comput.* **11**, 3696–3713 (2015).

68. Feenstra, K. A., Hess, B. & Berendsen, H. J. C. Improving efficiency of large time-scale molecular dynamics simulations of hydrogen-rich systems. *Journal of Computational Chemistry* **20**, 786–798 (1999).

69. Harvey, M. J., Giupponi, G. & Fabritiis, G. D. ACEMD: Accelerating Biomolecular Dynamics in the Microsecond Time Scale. *J. Chem. Theory Comput.* **5**, 1632–1639 (2009).

70. Harvey, M. J. & De Fabritiis, G. An Implementation of the Smooth Particle Mesh Ewald Method on GPU Hardware. *J Chem Theory Comput* **5**, 2371–2377 (2009).

71. Hopkins, C. W., Le Grand, S., Walker, R. C. & Roitberg, A. E. Long-Time-Step Molecular Dynamics through Hydrogen Mass Repartitioning. *J. Chem. Theory Comput.* **11**, 1864–1874 (2015).

72. Naritomi, Y. & Fuchigami, S. Slow dynamics of a protein backbone in molecular dynamics simulation revealed by time-structure based independent component analysis. *J Chem Phys* **139**, 215102 (2013).

73. Humphrey, W., Dalke, A. & Schulten, K. VMD: Visual molecular dynamics. *Journal of Molecular Graphics* **14**, 33–38 (1996).

74. Case, D. A. *et al*. *AMBER 2016*. (University of California, San Francisco, 2016).

75. Maier, J. A. *et al.* ff14SB: Improving the Accuracy of Protein Side Chain and Backbone Parameters from ff99SB. *J. Chem. Theory Comput.* **11**, 3696–3713 (2015).

76. Jorgensen, W. L., Chandrasekhar, J., Madura, J. D., Impey, R. W. & Klein, M. L. Comparison of simple potential functions for simulating liquid water. *J. Chem. Phys.* **79**, 926–935 (1983).

77. Götz, A. W. *et al*. Routine Microsecond Molecular Dynamics Simulations with AMBER on GPUs. 1. Generalized Born. *J. Chem. Theory Comput.* **8**, 1542–1555 (2012).

78. Salomon-Ferrer, R., Götz, A. W., Poole, D., Le Grand, S. & Walker, R. C. Routine Microsecond Molecular Dynamics Simulations with AMBER on GPUs. 2. Explicit Solvent Particle Mesh Ewald. *J. Chem. Theory Comput.* **9**, 3878–3888 (2013).

79. Le Grand, S., Götz, A. W. & Walker, R. C. SPFP: Speed without compromise—A mixed precision model for GPU accelerated molecular dynamics simulations. *Computer Physics Communications* **184**, 374–380 (2013).

80. Darden, T., York, D. & Pedersen, L. Particle mesh Ewald: An N·log(N) method for Ewald sums in large systems. *J. Chem. Phys.* **98**, 10089–10092 (1993).

81. Ryckaert, J.-P., Ciccotti, G. & Berendsen, H. J. C. Numerical integration of the cartesian equations of motion of a system with constraints: molecular dynamics of n-alkanes. *Journal of Computational Physics* **23**, 327–341 (1977).

82. Ozer, G., Quirk, S. & Hernandez, R. Adaptive steered molecular dynamics: validation of the selection criterion and benchmarking energetics in vacuum. *J Chem Phys* **136**, 215104 (2012).